THESIS FOR THE DEGREE OF DOCTOR OF PHILOSOPHY

Atomic-scale investigation of interfacial structures in WC-Co at finite temperatures

ERIK FRANSSON

Department of Physics

CHALMERS UNIVERSITY OF TECHNOLOGY

Göteborg, Sweden 2021

Atomic-scale investigation of interfacial
structures in WC-Co at finite temperatures
Erik Fransson

isbn 978-91-7905-523-3

Doktorsavhandlingar vid Chalmers tekniska högskola, Ny serie nr. 4990
issn 0346-718X

Department of Physics
Chalmers University of Technology
se-412 96 Göteborg, Sweden
Telephone +46 31 772 10 00

Cover: Atomic structure of a thin cubic film at the phase-boundary between WC and Co. Atomic structure generated with ase [1] and image rendered with ovito [2].

Chalmers digitaltryck
Göteborg, Sweden 2021

Atomic-scale investigation of interfacial structures in WC-Co at finite temperatures

Erik Fransson
Department of Physics
Chalmers University of Technology

Abstract

WC-Co cemented carbides combine superb hardness with high toughness making them ideal for usage in high-speed machining of steels and in wear resistance tools. These excellent mechanical properties are to a large extent dependent on the microstructure and thus the interfacial properties of the material. Hence, being able to predict and understand interfacial properties in this material can allow for, e.g., optimizing the manufacturing process in order to improve mechanical properties further.

Electronic structure calculations allow for accurately predicting interface energies for a given structure and composition. However, finding the ground-state interfacial structure and composition is challenging as the search space is very large when considering all degrees of freedom. Furthermore, direct sampling of interfacial properties at finite temperature using density functional theory (DFT) is usually computationally impractical as hundreds, thousands or even millions of calculations may be required. Therefore, employing atomic-scale models based on DFT calculations is advantageous and allows for investigation of the interface structure, composition and free energy at finite temperatures. In this thesis computational methods for calculating temperature-dependent interfacial free energies are developed and applied to the WC-Co system.

The emphasis is on understanding under which conditions cubic interfacial structures (complexions) can form on the WC basal plane in contact with Co. Configurational degrees of freedom are treated with cluster expansions and Monte Carlo simulations. Vibrational properties are mainly treated in the harmonic approximation using a regression approach to extract the harmonic force constants, which significantly reduces the number of DFT calculations. Interfacial phase diagrams are obtained for both the undoped WC-Co system and the Ti-doped system. Detailed information pertaining to structure and composition of the interfacial phases are obtained and show good agreement with experimental observations.

Keywords: cemented carbides, WC–Co, atomic-scale modeling, interfaces, complexions, free energies, phase diagrams, force constants, cluster expansions

LIST OF PUBLICATIONS

This thesis is partly based on the author's licentiate thesis (E. Fransson, *Computational investigation of interface structure and composition in cemented carbides at finite temperatures* (2019)) and the work presented in the following papers:

Method development

I **The Hiphive Package for the Extraction of High-Order Force Constants by Machine Learning**
Fredrik Eriksson, Erik Fransson and Paul Erhart
Advanced Theory and Simulations **2**, 1800184 (2019)

II **Efficient construction and applications of higher-order force constant models**
Erik Fransson, Fredrik Eriksson and Paul Erhart
npj Computational Materials **6**, 135 (2020)

III **icet – A Python library for constructing and sampling alloy cluster expansions**
Mattias Ångqvist, William A. Muñoz, J. Magnus Rahm, Erik Fransson, Céline Durniak, Piotr Rozyczko, Thomas Holm Rod, Paul Erhart
Advanced Theory and Simulations **2**, 1900015 (2019)

Applications

IV **A computational study of the temperature dependence of interface and surface energies in WC–Co cemented carbides**
Martin Gren, Erik Fransson, Göran Wahnström
International Journal of Refractory Metals and Hard Materials **87**, 105114 (2020)

V **Modeling of vibrational and configurational degrees of freedom in hexagonal and cubic tungsten carbide at high temperatures**
Martin Gren, Erik Fransson, Mattias Ångqvist, Paul Erhart, and Göran Wahnström
Physical Review Materials **5**, 033804 (2021)

VI **Complexions and grain growth retardation: First-principles modeling of phase boundaries in WC-Co cemented carbides at elevated temperatures**
Erik Fransson, Martin Gren and Göran Wahnström
Acta Materialia **216**, 117128 (2021)

VII **First-principles modeling of complexions at the phase-boundaries in Ti doped WC/Co at finite temperatures**
Erik Fransson, Martin Gren, Henrik Larsson and Göran Wahnström
Submitted to Physical Review Materials

Specification of the authors contribution to the publications:

I The author was part of developing the software HIPHIVE. The author carried out the nickel analysis in the paper.

II The author carried out most of the analysis for the applications and wrote the first draft of the paper.

III The author contributed to the development of the software ICET. The author helped with training of the cluster-expansions for the Ag–Pd application.

IV The author carried out most of the free energy calculations, except the ones concerning the solid-liquid interfaces. The development of the overall methodology and the analysis of the results were a joint effort. The author contributed to writing the paper.

V The author had the main responsibility for the atomistic modeling and the calculation of the free energies, except for configurational and electronic calculations. The development of the overall methodology and the analysis of the results were a joint effort. The author co-wrote the paper.

VI The author had the main responsibility for the atomistic modeling and the calculation of the free energies. The development of the overall methodology and the analysis of the results were a joint effort. The author was the main author of the paper.

VII The author had the main responsibility for the atomistic modeling and the calculation of the free energies. The development of the overall methodology and the analysis of the results were a joint effort. The author was the main author of the paper.

LIST OF PUBLICATIONS NOT INCLUDED IN THE PRESENT THESIS

I **Defects from phonons: Atomic transport by concerted motion in simple crystalline metals**
Erik Fransson and Paul Erhart
Acta Materialia **196**, 770 (2020)

II **dynasor – A tool for extracting dynamical structure factors and current correlation functions from molecular dynamics simulations**
Erik Fransson, Mattias Slabanja, Paul Erhart, Göran Wahnström
Advanced Theory and Simulations **4**, 2000240 (2021)

III **Thermal conductivity in intermetallic clathrates: A first-principles perspective**
Daniel O. Lindroth, Joakim Brorsson, Erik Fransson, Fredrik Eriksson, Anders Palmqvist, and Paul Erhart
Physical Review B **100**, 045206 (2019)

IV **Atomicrex – a general purpose tool for the construction of atomic interaction models**
Alexander Stukowski, Erik Fransson, Markus Mock and Paul Erhart
Modelling and Simulation in Materials Science and Engineering **25**, 055003 (2017)

V **A tale of two phase diagrams: Interplay of ordering and hydrogen uptake in Pd–Au–H**
Magnus Rahm, Joakim Löfgren, Erik Fransson, and Paul Erhart
Acta Materialia **211**, 116893 (2021)

VI **A Solution-Doped Polymer Semiconductor:Insulator Blend for Thermoelectrics**
David Kiefer, Liyang Yu, Erik Fransson, Andrés Gómez, Daniel Primetzhofer, Aram Amassian, Mariano Campoy-Quiles, and Christian Müller
Advanced Science **4**, 1600203 (2017)

VII **Extremely anisotropic van der Waals thermal conductors**
Shi En Kim, Fauzia Mujid, Akash Rai, Fredrik Eriksson, Joonki Suh, Preeti Poddar, Ariana Ray, Chibeom Park, Erik Fransson, Yu Zhong, David A. Muller, Paul Erhart, David G. Cahill, and Jiwoong Park
Nature, accepted (2021)

Acronyms

ABOP analytical bond order potential. 3, 36, 54

AIC Akaike information criteria. 19

ARDR automatic relevance detection regression. 19

BCC body-centered cubic. 38, 39

BIC Bayesian information criterion. 19

CE cluster expansion. 2, 4, 13–15, 19, 21, 22, 25–27, 35, 52, 54, 55, 57

CV cross-validation. 15, 16, 19, 20

DFT density functional theory. 1–4, 15, 26, 32, 33, 36, 49, 50, 54

DOF degree of freedom. 2, 8, 10, 13, 52, 54, 55, 57

EAM embedded atom method. 36, 39

EBSD electron backscatter diffraction. 44

ECI effective cluster interaction. 14, 15, 18

EHM effective harmonic model. 31–33, 55

EMT effective medium theory. 36

FCC face-centered cubic. 54

HRTEM high resolution transmission electron microscopy. 3, 47, 56

LASSO least absolute shrinkage and selection operator. 16, 17, 19, 20

MC Monte Carlo. 2, 4, 21–24, 54, 55

MD molecular dynamics. 2, 4, 31–33, 36, 37, 39, 40, 53, 55, 57

OLS ordinary least squares. 15–17, 19, 20

OMP orthogonal matching pursuit. 19

QHA quasi-harmonic approximation. 30

RFE recursive feature elimination. 19, 20

RMSE root-mean-square error. 15

SCP self-consistent phonons. 32

SGC semi-grand canonical. 55

TDEP temperature dependent effective potential. 31, 32

Contents

1 Introduction

1.1 Computational materials science

In computational materials science, models and simulations are employed in order to predict and understand properties of materials. This includes for example designing and discovering new materials with improved properties, providing explanations to experimental observations, and gaining fundamental understanding of the materials behavior. This is done at length scales ranging from nanometers to meters, and timescales between femtoseconds and hours.

The speed of computers has roughly doubled every two years for the last 50 or so years, which has been a huge driving force behind the development and success of computational materials science, complemented by improvements in algorithms and computational techniques. Additionally, the development of flexible and reliable software packages has been an important aspect in computational materials science.

1.2 First-principles techniques

At the smallest length- (nm) and time-scales (fs) quantum mechanical theories can be employed, which provide an accurate description based on the electronic structure of materials. Arguably the most popular computational method for solving the many-body quantum mechanical problem for electrons in condensed matter or chemistry is density functional theory (DFT) [3, 4]. DFT is a first-principles method, i.e. in principle no extra parameters apart from the atomic positions and numbers are needed to carry out calculations of electronic properties, such as the total energy of a system. In practice, one must resort, however, to an approximate description of the exchange-correlation contribution to the total energy.

DFT has been used throughout the years with great success and benefited greatly from the quick advances in both computational power and algorithms [5]. However, solving the quantum mechanical problem for electrons quickly becomes computationally expensive for large time-scales and when the number of atoms increases up to several hundreds due to poor scaling with number of electrons.

1.3 Finite temperatures

It is often desirable to be able to model and predict the properties of materials at finite temperatures. This usually requires evaluating thermodynamic averages over many degrees of freedom (DOFs), such as configurational DOFs (composition and order in the material) and vibrational DOFs (vibrational motion of atoms). This makes finite temperature properties difficult and often impossible to evaluate with DFT, as it may require many hundreds, thousands or millions of calculations. The computational cost of DFT calculations is thus often the limiting factor when trying to model and predict various properties at finite temperatures.

To overcome this problem, models for atomic interactions can be used, where electronic DOFs are simplified or neglected. Examples of atomic-scale models are interatomic potentials, cluster expansions (CEs), and force constant expansions. These models are trained from DFT and can thus effectively incorporate the effects from the electronic DOFs. They are often many orders of magnitude faster for evaluating the total energy of an atomic configuration compared to DFT while still retaining good accuracy. These models thus allow studying finite temperatures properties and can be used to access length and time scales up to μm and μs via methods such as molecular dynamics (MD) and Monte Carlo (MC) simulations.

There are of course limitations of atomic-scale models and it is crucial to understand under which conditions these models are accurate and under which they fail. The construction of these models is often non-trivial and can be a challenging task, especially with regard to the training process and understanding the transferability of the models. Additionally, when it comes to model construction, obtaining accurate models while reducing both human and computational time effort are important goals. Development of user friendly software packages to make atomic-scale model construction easier is therefore an integral part of the present thesis. In particular, the author contributed to the development of HIPHIVE for force constant potentials, presented in Papers I and II, and CEs presented in Paper III. In more recent years, machine learning approaches have become more popular in atomic-scale modeling and computational materials science in general for e.g. high-throughput searches [6, 7].

1.4 Cemented carbides

Cemented carbides, or hard metals, is a class of materials which consists of fine particles of a carbide, often WC, cemented into a composite with a binder metal, often Co [8, 9, 10]. They combine excellent hardness with high toughness and wear resistance, making them ideal materials for cutting and wear resistant tools [11, 12]. The unique mechanical properties of cemented carbides derive from their microstructure [13]. The microstructure is largely dependent on interfacial properties when sintering the material at up to 1700 K. Understanding the interfacial properties of cemented carbides is therefore of importance in order to be able to design a desirable material.

The main WC phase is the hexagonal phase, referred to as δ-WC. At high temperatures, 3000 K, a cubic phase becomes stable referred to as γ-WC. In Paper V we studied the free energies of these two WC phases as a function of temperature and carbon content. The obtained phase transition is within 10% of the experimentally observed transition temperature which validates our atomic-scale approach. Furthermore, having a detailed understanding the free energy contributions of these two phases prove useful when it comes to modeling the free energies of more difficult systems such as interfaces in WC–Co.

Interface energies in WC–Co have been extensively studied at 0 K using DFT calculations [14, 15, 16, 17, 18, 19]. In Paper IV, the temperature dependence of the energetics of a few typical interfaces (surfaces, grain boundaries and phase boundaries) in WC–Co cemented carbide was studied using an analytical bond order potential (ABOP). This is done as a function of temperature up to and beyond the melting point of Co.

In Paper VI, the formation of thin cubic WC films at the phase boundary between hexagonal WC phase and Co phase was studied. We constructed an interfacial phase diagram showing under which conditions the cubic films are stable, enabling a discussion of how these films may influence the grain growth in cemented carbides. In Paper VII, we carried out a similar study of the formation of Ti-rich cubic films at WC–Co phase boundaries. The calculated interfacial phase diagram is coupled to thermodynamic databases in order to make the results more relevant for experimental comparisons. We also find that Ti atoms only segregate to the inner metallic layer of the thin cubic film leaving an almost pure W layer towards Co, an arrangement that has been observed in recent experimental high resolution transmission electron microscopy (HRTEM) studies.

1.5 Aim and outline of thesis

The present thesis focuses on constructing atomic-scale models and using them to sample finite temperature properties and free energies for interface systems in cemented carbides. This has been carried out using various types of atomic-scale models, the con-

struction of which was enabled by the development of the software packages HIPHIVE and ICET.

Chapter 2 provides an overview of the statistical physics concepts used in the present thesis is given, with a focus on how thermodynamics can be simplified when considering solids. Alloy CEs and their construction using DFT data are introduced in Chapter 3. Additionally, free energy sampling using MC simulations is discussed and demonstrated by examples. Chapter 4 introduces force constant models and describes their application for extracting thermodynamic properties and free energies. Chapter 5 presents a brief overview of interatomic potentials and how they can be used for carrying out MD simulations. Chapter 6 provides an introduction to cemented carbides. The papers included in this thesis are briefly summarized in Chapter 7 and the thesis is concluded with an outlook in Chapter 8.

2

Thermodynamics and statistical physics

In this chapter a brief overview of classical thermodynamics and statistical physics will be given based on literature [20, 21, 22].

2.1 Ensembles

Statistical physics provides a way for relating the microscopic properties of particles to the macroscopic thermodynamic properties of materials and large systems. An ensemble is a collection of identical systems with the same macroscopic properties, but can occupy different microscopic states. The ensemble of systems provides a probability distribution for the system to occupy any given microscopic state, and allows us to compute averages over the ensemble.

We start by defining the the positions of N classical particles as $\boldsymbol{r} = \left(\boldsymbol{r}_1, \boldsymbol{r}_2, \ldots \boldsymbol{r}_N\right)$, and analogously the momenta $\boldsymbol{p} = \left(\boldsymbol{p}_1, \boldsymbol{p}_2, \ldots \boldsymbol{p}_N\right)$. A set of positions and velocities, $(\boldsymbol{r}, \boldsymbol{p})$, defines a microstate. We let $\mathscr{H}$ denote the Hamiltonian, i.e. the energy of a system is given by $E = \mathscr{H}(\boldsymbol{r}, \boldsymbol{p})$. For the sake of simplicity, here, we will only consider identical particles. The generalization to a multicomponent system is straight forward, as N and μ would be replaced with, e.g., N_A, N_B and μ_A, μ_B, respectively.

2.1.1 Microcanonical ensemble

First we consider the microcanonical ensemble, corresponding to an isolated system with fixed number of particles, N, volume V, and energy E. We assume that all microstates are equally probable in this ensemble. This means the probability for a partic-

ular microstate is $1/\Omega(N, V, E)$, where $\Omega(N, V, E)$ is the total number of states for the given macroscopic parameters N, V, E. The number of states, $\Omega(N, V, E)$, is given by

$$\Omega(N, V, E) = \frac{E_0}{N!} \iint \frac{\mathrm{d}\boldsymbol{r}\mathrm{d}\boldsymbol{p}}{h^{3N}} \delta(\mathscr{H}(\boldsymbol{r}, \boldsymbol{p}) - E), \tag{2.1}$$

where the integrals extend over all possible positions, $\boldsymbol{r}$, and momenta, $\boldsymbol{p}$, in the volume, V, and the delta function filters out the states with an energy not equal to E. The occurrence of Planck's constant, h, in the prefactor reflects the fact that the phase space volume of a single microstate is h^{3N} such that the division with h^{3N} yields the number of microstates. Here, E_0 defines the accuracy for which the energy of a microstate can be determined, and renders $\Omega(N, V, E)$ dimensionless. The $1/N!$ term compensates for the overcounting of identical microstates due to permutations of particle indices.

The number of states is connected to thermodynamics via Boltzmann's entropy formula

$$S(N, V, E) = k_\mathrm{B} \ln \Omega(N, V, E), \tag{2.2}$$

where $S(N, V, E)$ is the entropy of the system and k_B is Boltzmann's constant. The microcanonical ensemble serves as a starting point for the derivation of other ensembles.

2.1.2 Canonical ensemble

In the canonical ensemble, the system is assumed to be in thermal equilibrium with a reservoir, such that the system and the reservoir can freely exchange heat. The number of particles, N, volume, V and temperature, T, of the system are kept constant. The energy of the system E may, however, fluctuate due to heat exchange with the reservoir. The probability of observing a microstate with energy E is $P \propto \mathrm{e}^{-\beta E}/Z$, where $\beta = 1/k_\mathrm{B}T$ and Z is the canonical partition function

$$Z(N, V, T) = \frac{1}{E_0} \int_0^\infty \mathrm{d}E\, \mathrm{e}^{-\beta E}\, \Omega(N, V, E) = \frac{1}{N!} \iint \frac{\mathrm{d}\boldsymbol{r}\mathrm{d}\boldsymbol{p}}{h^{3N}} \mathrm{e}^{-\beta \mathscr{H}(\boldsymbol{r}, \boldsymbol{p})}. \tag{2.3}$$

From the partition function thermodynamics averages, $\langle \ldots \rangle$, of some property $A(\boldsymbol{r}, \boldsymbol{p})$ can be evaluated as

$$\langle A \rangle = \frac{\iint \mathrm{d}\boldsymbol{r}\mathrm{d}\boldsymbol{p}\, A(\boldsymbol{r}, \boldsymbol{p}) \mathrm{e}^{-\beta \mathscr{H}(\boldsymbol{r}, \boldsymbol{p})}}{\iint \mathrm{d}\boldsymbol{r}\mathrm{d}\boldsymbol{p}\, \mathrm{e}^{-\beta \mathscr{H}(\boldsymbol{r}, \boldsymbol{p})}}. \tag{2.4}$$

The fluctuations (variance) of the energy, $(\Delta E)^2 = \left\langle E^2 \right\rangle - \langle E \rangle^2$, can be evaluated via Eq. (2.4) yielding the relation

$$C_V = \frac{(\Delta E)^2}{k_B T^2}, \tag{2.5}$$

where C_V is the heat capacity of the system. Because C_V and E scale linearly with N, the fluctuations of the energy, ΔE, per particle will tend to zero, $\Delta E/N \to 0$, as $N \to \infty$ [22].

The partition function is related to the thermodynamic potential, the Helmholtz free energy $F = E - TS$, as

$$F(N,V,T) = -\frac{1}{\beta} \ln Z(N,V,T). \tag{2.6}$$

In a quantum mechanical treatment, the Hamiltonian is replaced with an operator $\mathscr{H} \to \hat{\mathscr{H}}$, and the canonical partition function becomes

$$\iint \frac{\mathrm{d}\boldsymbol{r}\mathrm{d}\boldsymbol{p}}{h^{3N}} \mathrm{e}^{-\beta\mathscr{H}(\boldsymbol{r},\boldsymbol{p})} \to \sum_i \mathrm{e}^{-\beta E_i}, \tag{2.7}$$

where the summation runs over all eigenstates of $\hat{\mathscr{H}}$. Once the quantum mechanical partition function is known, the thermodynamics can be described analogously to the classical case [22].

2.1.3 Isothermal–isobaric ensemble

In the isothermal–isobaric ensemble the number of particles, N, pressure, P, and temperature, T, are kept fixed. In this ensemble the system can exchange both heat and volume with a reservoir. The corresponding partition function is given by

$$\mathscr{Z}(N,P,T) = \frac{1}{V_0}\int_0^\infty dV \mathrm{e}^{-\beta PV} Z(N,V,T) = \frac{1}{V_0}\int_0^\infty dV \mathrm{e}^{-\beta[F(N,V,T)+PV]}, \tag{2.8}$$

where V_0 is a normalization constant. The partition function is related to Gibbs free energy via

$$G(N,P,T) = -\frac{1}{\beta} \ln \mathscr{Z}(N,P,T), \tag{2.9}$$

where $G = F + PV = E - TS + PV$.

The fluctuations of the volume, $(\Delta V)^2 = \left\langle V^2 \right\rangle - \langle V \rangle^2$, can be evaluated analogously to the fluctuations of the energy in the canonical ensemble. The volume fluctuation per particle will approach zero, $\Delta V/N \to 0$, in the thermodynamic limit, $N \to \infty$. This means that the Gibbs free energy can be calculated as

$$G(N,P,T) = \min_V \left[F(N,V,T) + PV\right], \tag{2.10}$$

where the minimization is carried out with respect to the volume, V.

2.1.4 Grand canonical ensemble

Lastly, the grand canonical ensemble will be considered. In this ensemble the chemical potential μ, volume V and temperature T are kept fixed. Here, the system can exchange both heat and particles with a reservoir. Similarly to the isothermal-isobaric (NPT) ensemble, the partition function can be expressed in terms of the canonical partition function as

$$\mathcal{Z}(\mu, V, T) = \sum_{N=0}^{\infty} \mathrm{e}^{\beta\mu N} Z(N, V, T) = \sum_{N=0}^{\infty} \mathrm{e}^{-\beta[F(N,V,T)-\mu N]}, \tag{2.11}$$

where the summation runs over the number of particles, N. The partition function is related to the grand canonical potential, $\Phi(\mu, V, T) = F - \mu N = E - TS - \mu N$, via

$$\Phi(\mu, V, T) = -\frac{1}{\beta} \ln \mathcal{Z}(\mu, V, T). \tag{2.12}$$

In this ensemble the thermodynamic average of the number of particles, $\langle N \rangle$, and variance $(\Delta N)^2$ can be evaluated. Here, we obtain that $(\Delta N)/\langle N \rangle \to 0$ as $V \to \infty$. This allows the grand-canonical potential to be obtained via

$$\Phi(\mu, V, T) = \min_{N} \left[F(N, V, T) - \mu N \right]. \tag{2.13}$$

2.2 Solids

Next, we will see how some of the thermodynamics can be simplified if we restrict ourselves to consider periodic solids. We consider a solid for which the atoms occupy a lattice, as shown schematically in Fig. 2.1a). The lattice sites are denoted $\boldsymbol{r}_0$, which describes the positions of the N lattice sites. We let $\boldsymbol{\sigma}$ denote the occupation vector of the lattice, describing which atom types occupy which lattice sites as shown in Fig. 2.1b). Finally, we let $\boldsymbol{r}$ denote the positions of the N atoms in the system. Here, it is often convenient to work with the displacements from the lattice sites, $\boldsymbol{u} = \boldsymbol{r} - \boldsymbol{r}_0$.

2.2.1 Canonical ensemble for a lattice

First, we consider the canonical ensemble for a particular lattice, α. In this case the partition function, Eq. (2.3), can be limited to only include microstates that correspond to said lattice. Further, the partition function can be coarse-grained since the vibrational motion, i.e. changes in $\boldsymbol{u}$, is typically much faster than the configurational DOFs, i.e. changes in $\boldsymbol{\sigma}$. This allows us to write the partition function, $Z_\alpha(N, V, T)$, as a double sum

$$Z(N, V, T)_\alpha = \sum_{\text{conf}} \mathrm{e}^{-\beta U(\boldsymbol{\sigma})} \sum_{\text{vib}} \mathrm{e}^{-\beta E_{\boldsymbol{\sigma}}(\boldsymbol{u})}, \tag{2.14}$$

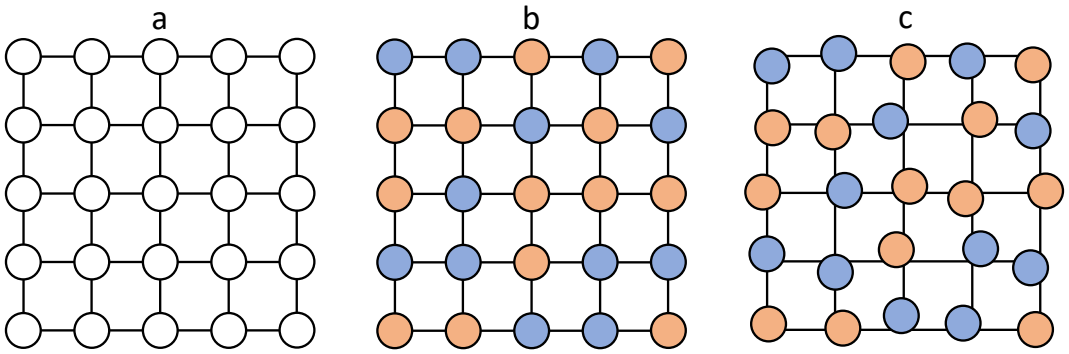

Figure 2.1: a) Illustration of a two dimensional cubic lattice with positions $\boldsymbol{r}_0$. b) The lattice occupied by two atom types (blue and orange) described by the occupation vector $\boldsymbol{\sigma}$. c) The atoms are displaced from the lattice sites with displacement vector $\boldsymbol{u}$.

where the first sum runs over all possible occupation vectors (consistent with the number of atoms of each species) and the second one over all vibrational states associated with $\boldsymbol{\sigma}$ [23, 24]. Here $U(\boldsymbol{\sigma})$ describes the potential energy with $\boldsymbol{u} = 0$ and $E_{\boldsymbol{\sigma}}(\boldsymbol{u})$ describes the kinetic and the additional potential energy associated with the displacements for the specific configuration $\boldsymbol{\sigma}$. The vibrational states associated with a configuration are not strictly defined, but one should consider displacements, $\boldsymbol{u}$, smaller than some fraction of the nearest neighbor distance of the lattice.

This coarse graining of the partition function is schematically visualized in Fig. 2.2. Here, each configuration has a potential energy landscape described by a $U_{\boldsymbol{\sigma}}(\boldsymbol{u})$ (dashed lines), which are treated independently. We let $Z_\alpha^{\text{vib}}(N, V, T, \boldsymbol{\sigma})$ denote the vibrational partition function for configuration $\boldsymbol{\sigma}$ defined as the second sum in Eq. (2.14). This allows us to define a vibrational free energy for a given configuration, according to Eq. (2.6), as $F_{\text{vib}}(\boldsymbol{\sigma}) = -\frac{1}{\beta} \ln Z_\alpha^{\text{vib}}(\boldsymbol{\sigma})$. Finally, we can rewrite Eq. (2.14) as

$$Z_\alpha(N, V, T) = \sum_{\text{conf}} \mathrm{e}^{-\beta[U(\boldsymbol{\sigma}) + F_{\text{vib}}(\boldsymbol{\sigma})]}. \tag{2.15}$$

2.2.2 Approximations

In practice, evaluating Eq. (2.15) is still quite difficult, and various types of approximations can be made. For example, hexagonal WC is practically always very close to its stoichiometric composition and can therefore be approximated as only having one relevant configuration. In these type of cases, the sum in Eq. (2.15) can be removed and the vibrational free energy only needs to be calculated for a single configuration. The

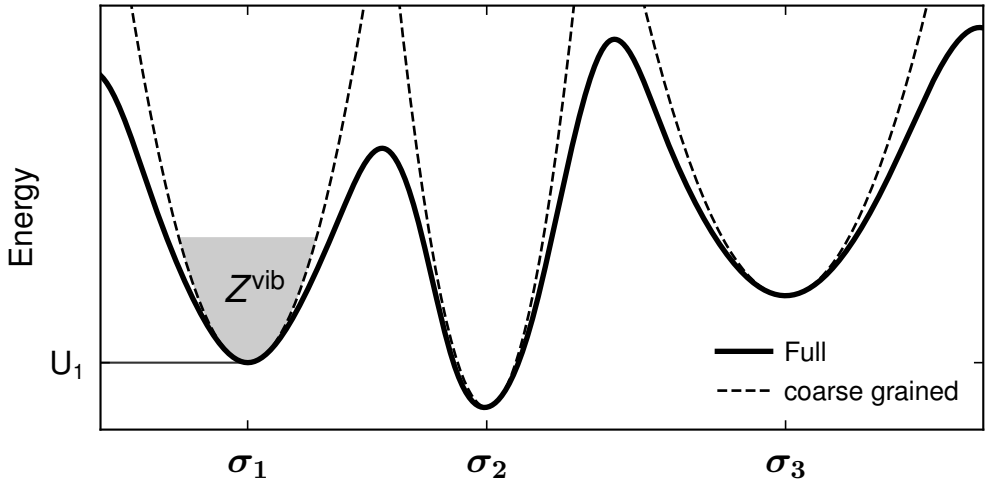

Figure 2.2: Schematic representation of the full potential energy landscape, $U(\boldsymbol{r})$, and how it can be decomposed by occupation, $\boldsymbol{\sigma}$, and the associated displacements for each configuration, $\boldsymbol{u}$. The shaded region schematically indicates the vibrational states associated with $\boldsymbol{\sigma}_1$.

small amount of vacancies present in hexagonal WC (less than 1%) can be included in the dilute limit approximation, see Sect. 2.2.3, which is demonstrated in Paper V.

Cubic WC, on the other hand, contains up to about 50% carbon vacancies and therefore both the configurational and vibrational DOFs must be included in the partition function. In Papers VI and VII this is accomplished by calculating the vibrational free energy for the ground-state configuration, $\boldsymbol{\sigma}_{\mathrm{GS}}$, which minimizes $U(\boldsymbol{\sigma})$. Then, the vibrational free energy is approximated as being $\boldsymbol{\sigma}$ independent, i.e. $F_{\mathrm{vib}}(\boldsymbol{\sigma}) \approx F_{\mathrm{vib}}(\boldsymbol{\sigma}_{\mathrm{GS}})$. In Paper V we take this approach one step further and calculate $F_{\mathrm{vib}}(\boldsymbol{\sigma})$ for a few typical configurations (representative structures), $\boldsymbol{\sigma}_{\mathrm{RS}}$, which gives a better estimate of Eq. (2.15).

2.2.3 Defects in the dilute limit

Real solids contain defects. In the dilute limit, i.e. at low defect concentrations, the defects can be treated as non-interacting, which allows one to approximate the canonical free energy of the system [25].

Let us consider a lattice with N_0 sites with n_{vac} vacancies where $N_0 \gg n_{\mathrm{vac}}$. We denote the change in energy and vibrational free energy when introducing a single vacancy as ΔF_{vac}. In the dilute limit the energy of a configuration with n_{vac} vacancies is the same, independent of how the vacancies occupy the lattice. This means that

the terms in the sum from Eq. (2.15) are identical and the canonical free energy of the system with n_{vac} vacancies can be written as

$$F(n_{\text{vac}}) = F(0) + n_{\text{vac}}\Delta F_{\text{vac}} - k_{\text{B}}T \ln \binom{N_0}{n_{\text{vac}}}, \tag{2.16}$$

where $\binom{N_0}{n_{\text{vac}}}$ is the number of terms in summation in Eq. (2.15), i.e. the number of possible ways to distribute n_{vac} vacancies on N_0 lattice sites. The term $k_{\text{B}} \ln \binom{N_0}{n_{\text{vac}}}$ corresponds to the configurational entropy, S_{conf}, and if evaluated using Stirling's approximation for $n_{\text{vac}} \ll N_0$ one obtains

$$S_{\text{conf}} = -N_0 k_{\text{B}} \left[x \ln x + (1-x) \ln (1-x) \right], \tag{2.17}$$

where $x = n_{\text{vac}}/N_0$ is the vacancy concentration. Now, the canonical free energy for the lattice with n_{vac} vacancies, $F(n_{\text{vac}})$, is known. In practice one often also includes the change in volume due to introducing a vacancy resulting in a $P\Delta V$ term, but neglected here for simplicity's sake.

Next, we can use $F(n_{\text{vac}})$ to extract the equilibrium vacancy concentration, x_{eq}, in the system given some reference chemical potential μ (which for a single component system often is $F(0)/N_0$) using Eq. (2.13). The minimum of grand potential, Φ, can be obtained by differentiation, which yields

$$x_{\text{eq}} = \mathrm{e}^{-\beta(\Delta F_{\text{vac}} + \mu)}, \tag{2.18}$$

where $\Delta F_{\text{vac}} + \mu$ is commonly referred to the vacancy formation free energy, $\Delta G_{\text{f}}^{\text{vac}}$.

2.2.4 Interfaces

For interfaces we can define the interface free energy, γ, corresponding to the cost associated with creating the interface per area. This is done by considering the free energy of the interface system relative to the free energy of some reference states, and γ is defined as

$$\gamma(T) = \frac{1}{A}\Big(G_{\text{int}}(T) - \sum_i N_i \mu_i(T) \Big), \tag{2.19}$$

where G_{int} is the Gibbs free energy for the interface system, A the area of the interface, and N_i and μ_i are the number of atoms and chemical potential of each atom type, respectively [26]. The chemical potentials, μ_i, are free energies for some reference states thought to be in equilibrium with the interface system. This allows us to also

decompose the interface free energy into configurational and vibrational contributions. This is done in Papers VI and VII, and, for example, the vibrational part becomes

$$\gamma_{\mathrm{vib}}(T) = \frac{1}{A}\left(G_{\mathrm{int}}^{\mathrm{vib}}(T) - \sum_i N_i \mu_i^{\mathrm{vib}}(T)\right). \tag{2.20}$$

This type of decomposition can further help understanding which contributions are important for interface energies, defect formation energies, and phase stability.

3

Alloy cluster expansions

One of the most common techniques for modeling the configurational DOFs of multi-component systems is the so-called alloy CE approach. It is based on a static lattice where the DOFs are the occupations of the lattice, meaning it can model the potential energy for configurations, i.e., $U(\boldsymbol{\sigma})$. The main idea is to decompose an atomic structure into its corresponding clusters (pairs, triplets etc). Associating each clusters with an energy then allows for predicting the total energy of any structure based on the same lattice. The prediction of total energies using CEs is very fast, which enables one to study the thermodynamics of systems with a large number of configurational DOFs by statistical sampling.

3.1 Clusters

An atomic structure can be described by a set of lattice points, a cell and an occupation vector $\boldsymbol{\sigma}$ that specifies which atomic species occupies which lattice point, as discussed in Sect. 2.2. A cluster is defined as a collection of unique lattice points, where the number of lattice points defines the order of the cluster. For example a cluster of two lattice points corresponds to a pair, i.e. a second order cluster. Clusters can be grouped into orbits or neighbor shells, i.e., first nearest neighbor pairs, second nearest neighbor pairs and so on. This can easily be imagined for simple lattices, such as the simple square one illustrated in Fig. 3.1, whereas for more complex systems and higher order clusters it is more complicated to construct orbits of clusters. The definition of an orbit used here (and in ICET and HIPHIVE) is the collection of all symmetrically equivalent clusters. Two clusters are considered equivalent if they can be transformed into each other by any combination of the symmetry operations of the underlying lattice, where a symmetry operation consists of a rotation $\boldsymbol{R}$ and a translation $\boldsymbol{t}$. Applying a lattice

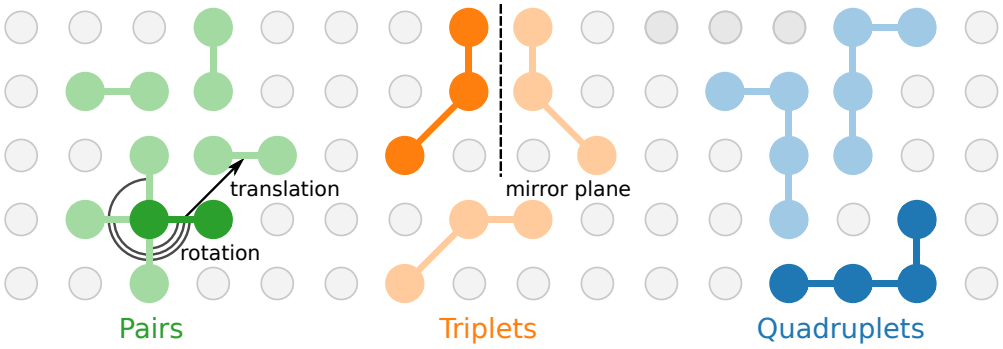

Figure 3.1: Illustration of a simple square lattice with pairs (green), triplets (orange) and quadruplets (blue) highlighted. All clusters of the same order can be transformed into each other using the symmetry operations of the underlying lattice, a few of which are illustrated.

symmetry to lattice point coordinate $\boldsymbol{r}$ is done via

$$\tilde{\boldsymbol{r}} = \boldsymbol{R} \cdot \boldsymbol{r} + \boldsymbol{t}, \tag{3.1}$$

where $\tilde{\boldsymbol{r}}$ is the position of a new lattice point. Subjecting all lattice points to a symmetry operation leaves the lattice unchanged (save a permutation of ordering of lattice points). If lattice points (i, j) are mapped to lattice points (k, l) using the symmetry operation number s, e.g.

$$(i, j) \xrightarrow{\boldsymbol{R}_s, \boldsymbol{t}_s} (k, l) \tag{3.2}$$

then the pair (i, j) is said to be symmetry equivalent to the (k, l) pair, and they therefore belong to the same orbit. This is illustrated in Fig. 3.1, where all highlighted clusters of the same order are symmetrically equivalent.

3.2 Formalism

CEs can describe any property which is a function of the occupation $\boldsymbol{\sigma}$ of the lattice. Here, we will consider a CE for the potential energy of a configuration, $U(\boldsymbol{\sigma})$, as

$$U(\boldsymbol{\sigma}) = U_0 + \sum_{\boldsymbol{\alpha}} \langle \Pi_{\boldsymbol{\alpha}'}(\boldsymbol{\sigma}) \rangle_{\boldsymbol{\alpha}} \, m_{\boldsymbol{\alpha}} J_{\boldsymbol{\alpha}}, \tag{3.3}$$

where $\Pi_{\boldsymbol{\alpha}}$ are basis functions, $m_{\boldsymbol{\alpha}}$ the multiplicity, $J_{\boldsymbol{\alpha}}$ are the effective cluster interactions (ECIs) and the summation goes over all distinct clusters. The full formalism can be found in Paper III and in Ref. 27.

In order to find the unknown parameters of the model $\boldsymbol{J}_{\boldsymbol{\alpha}}$, training structures are required. For training structure i with occupation $\boldsymbol{\sigma}_i$ and energy E the cluster vector can be constructed via

$$\boldsymbol{\Pi}_i = (1, \langle \Pi_{\boldsymbol{\alpha}'}(\boldsymbol{\sigma}_i) \rangle_{\boldsymbol{\alpha}} \, m_{\boldsymbol{\alpha}}), \tag{3.4}$$

where $\boldsymbol{\Pi}_i$ refers to the cluster vector of structure i and the starting 1 is included in order to pick up the first (constant) term in Eq. (3.3). This yields a linear system of equations

$$\boldsymbol{E} = \boldsymbol{\Pi} \boldsymbol{J}, \tag{3.5}$$

where $\boldsymbol{E}$ is the target energies for all structures and $\boldsymbol{\Pi}$ is a matrix where each row corresponds to the cluster-vector for a structure. This linear system of equations can be solved for the ECIs $\boldsymbol{J}$.

In principle, the summation in Eq. (3.3) extends over an infinite number of clusters, however, in practice the summation must be truncated. This is usually done by imposing a cutoff, meaning that ECIs corresponding to clusters with interatomic distances larger than the cutoff are zero. Additionally, the summation can be truncated with respect to the order of clusters, for example, we might include pairs and triplets in the CE but not quadruplets (or higher-order clusters).

3.3 Linear regression

It is often desirable to solve the linear problem with as few training structures as possible because evaluating their energies with DFT is computationally expensive. There are many different linear regression methods one can employ to solve Eq. (3.5). The simplest approach is to use ordinary least squares (OLS), which minimizes the root-mean-square error (RMSE) for the training structures. The RMSE is defined as

$$\mathrm{RMSE} = \sqrt{\frac{1}{N} \sum_{i}^{N} \left(E_i^{\mathrm{target}} - E_i^{\mathrm{predicted}} \right)^2}, \tag{3.6}$$

where the summation is carried out over N structures.

3.3.1 Cross-validation

Cross-validation (CV) is a way of statistically testing the accuracy of a model trained on a given dataset. The dataset is the collection of structures with known energies, $\boldsymbol{D} = \left[(\boldsymbol{\Pi}_1, E_1), \ldots, (\boldsymbol{\Pi}_N, E_N) \right]$. In CV the dataset, $\boldsymbol{D}$, is split into two parts: one used for training (training set) and one used for validating the model (validation set). This

is repeated multiple times with different splits of the dataset in order to reduce the statistical noise. One of the more common ways of splitting the data is the k-fold method where the dataset is split into k equally large parts. The training is done using $k-1$ parts and the last part of the dataset is used for validation, which can be repeated k times. CV can, for example, be used to optimize hyperparameters of the model, such as cutoffs or regularization parameters.

3.3.2 Regularization

Even if the linear system of equations is overdetermined, OLS tends to lead to overfitting, meaning the model learns too many details in the training set, which causes larger errors for structures not present in the training set. Overfitting is commonly combatted by regularization, i.e., addition of a penalty term in the objective function

$$\|\boldsymbol{\Pi}\boldsymbol{J}-\boldsymbol{E}\|_2^2+\alpha\|\boldsymbol{J}\|_1+\beta\|\boldsymbol{J}\|_2^2, \tag{3.7}$$

where the first term is the objective function for OLS and the last two terms are ℓ_1 and ℓ_2 regularization terms where α and β control their respective strengths [28]. The parameters are found by minimizing the objective function with respect to $\boldsymbol{J}$. Setting $\beta=0$ yields the objective function of least absolute shrinkage and selection operator (LASSO), which tends to favor sparse solution vectors $\boldsymbol{J}$. For $\alpha=0$ one recovers the objective function for ridge which penalizes large elements in $\boldsymbol{J}$ and tries to keep all parameters small. Determining suitable values for α and β can be done, e.g., via CV or a Bayesian approach [29].

An example of the effect from regularization is shown in Fig. 3.2. Here, an eighth-order polynomial is fitted as a linear problem using ten training samples generated from a polynomial (the true model) with the addition of small noise. The model obtained with OLS describes all training samples very well, whereas in the regions between training samples the model exhibits large fluctuations and performs poorly compared to the true model, a clear indication of overfitting. Both ridge and LASSO generate less complex models and consequently generalize better to regions where no training data exists. Here the regularization parameters α and β for LASSO and ridge were found by CV analysis.

3.3.3 Probabilistic models

One can also take a Bayesian parameter estimation approach to the linear problem based on Bayes theorem. The idea is to define a probability distribution (posterior), $P(\boldsymbol{J}\,|\,D)$, for the unknown parameters $\boldsymbol{J}$, given the data $\boldsymbol{D}$ and prior information as

$$P(\boldsymbol{J}\,|\,D)=\frac{P(D|\boldsymbol{J})P(\boldsymbol{J})}{P(D)}, \tag{3.8}$$

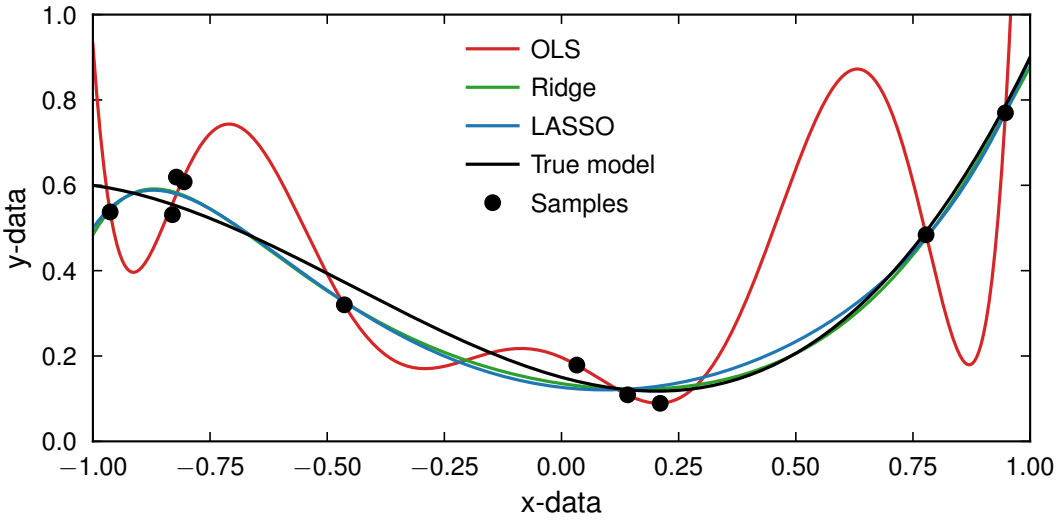

Figure 3.2: Illustration of fitting a polynomial to training data generated from the true model with added noise. The OLS model shows clear signs of overfitting, whereas the models constructed with LASSO and ridge perform better.

where $P(D|\boldsymbol{J})$ and $P(\boldsymbol{J})$ are commonly referred to as the likelihood and the prior, respectively. Here, the normalization $P(D)$ can often be ignored. By generating models, $\boldsymbol{J}$, drawn from the posterior, $P(\boldsymbol{J}|D)$, one can obtain probability distributions for various properties of the model (such as the energy of a structure).

Next, we will consider the same example as in Fig. 3.2, but solve it with a Bayesian approach. Here, a simple likelihood and prior are employed as

$$P(D|\boldsymbol{J}) \propto \exp\left[-\frac{\|\boldsymbol{\Pi}\boldsymbol{J}-\boldsymbol{E}\|_2^2}{2\sigma}\right] \tag{3.9}$$

$$P(\boldsymbol{J}) \propto \exp\left[-\frac{\|\boldsymbol{J}\|_2^2}{2\lambda}\right], \tag{3.10}$$

which corresponds to assuming that errors are independent and identically normally distributed with zero mean and standard deviation σ and a normal distribution as prior with zero mean and standard deviation λ for each parameter. With the likelihood and priors defined, models can be drawn from the posterior probability distribution Eq. (3.8) and used to make predictions as shown in Fig. 3.3. The average prediction agrees well with the true model. Further, the standard deviation provides insight into the uncertainty of our model, and as expected the standard deviation is larger in regions where no training samples are available.

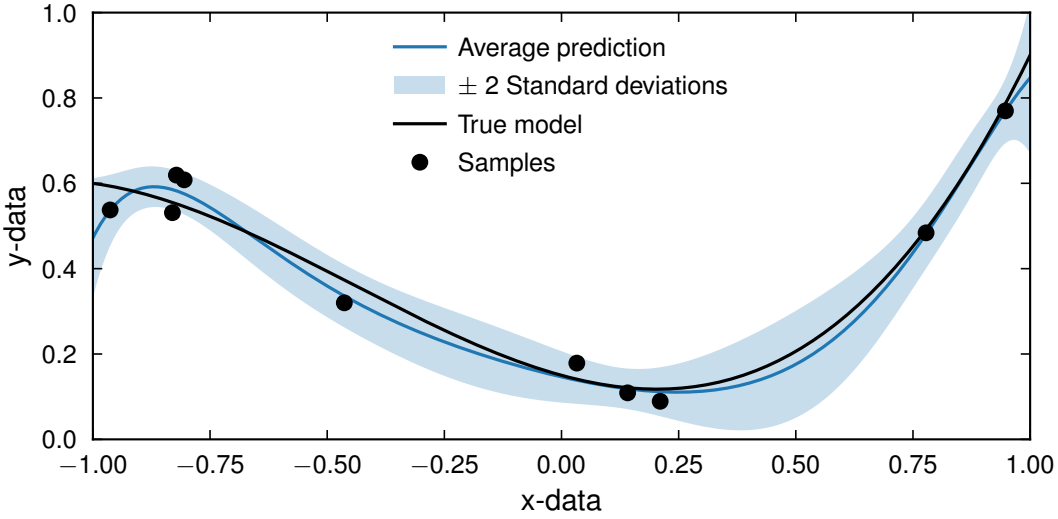

Figure 3.3: Illustration of Bayesian fitting of a polynomial to training data generated from the true model and a addition of noise using the same data as in Fig. 3.2. Here the average prediction corresponds to the average prediction from models drawn from the posterior $P(\boldsymbol{J}\,|\,D)$. The standard deviation of these predictions are shown as the shaded region. Note that the standard deviation shown does not include the error σ.

The Bayesian approach can also provide a useful interpretation of the linear regression problem. The model that maximizes the posterior (maximum a posteriori), $\boldsymbol{J}_{\text{opt}}$, can be found from maximizing $\log\left[P(D|\boldsymbol{J})P(\boldsymbol{J})\right]$. Using the likelihood and priors in the example above, Eq. (3.10), we obtain

$$\boldsymbol{J}_{\text{opt}} = \underset{\boldsymbol{J}}{\text{argmin}} \left\{ \frac{\|\boldsymbol{\Pi}\boldsymbol{J} - \boldsymbol{E}\|_2^2}{2\sigma} + \frac{\|\boldsymbol{J}\|_2^2}{2\lambda} \right\}, \tag{3.11}$$

where the maximization has been turned into a minimization by introducing a minus sign. This minimization is exactly equivalent to ridge regression [28], see Eq. (3.7). From this we can thus interpret the regularization terms as prior probabilities for parameters. In the Bayesian approach one can thus encode physical intuition about the parameters, $\boldsymbol{J}$, in the prior, $P(\boldsymbol{J})$. For example, this could be properties like interaction strength decaying with interatomic distance or that similar clusters ought to have similar ECIs as demonstrated in Ref. 30.

An alternative approach to generate a collection of models is to construct models from different splits of the training structures. This is done by randomly including N structures in the training set with replacement, i.e., allowing for duplicates in the

training set. This can be repeated multiple times in order to generate multiple different training sets and subsequently multiple different models, and is known as bootstrapping or bagging [31]. This is demonstrated for phase diagram construction and chemical ordering analysis in Paper III, and for phonon properties in Paper II. This approach was also recently employed to estimate the uncertainty of predicted energies for CEs in order to effectively generate good training structures [32].

3.3.4 Feature selection

Feature selection is the process of finding the most important parameters (features) during model construction, and discarding the rest. Reducing the number of non-zero parameters yields a less complex model, which often leads to less overfitting.

Compressive sensing algorithms, commonly used in signal processing [33], have been proposed to be suitable for constructing physical (sparse) models [34, 29]. In these algorithms ℓ_1 regularization is used, similar to LASSO.

There are also other feature selection algorithms for linear problems such as recursive feature elimination (RFE), orthogonal matching pursuit (OMP) and automatic relevance detection regression (ARDR). In RFE one first trains a model using all features and then removes the least important one, where importance could be measured as the absolute value of the parameter. This process is repeated until the desired number of features is left. OMP works similarly but instead starts out without any features and then iteratively adds the most important feature until the desired number of features is reached. ARDR is Bayesian algorithm where each parameter has a normal prior with a standard deviation λ_i for parameter i. The standard deviations are iteratively updated and if λ_i becomes too small, indicating a narrow distribution around zero, the parameter is pruned from the model.

For all the feature selection methods mentioned above there is one or more hyperparameters controlling the number of non-zero parameters in the model. The number of features that are suitable to keep in a model can be evaluated using CV. Additionally, this can be done using information criteria such as Akaike information criteria (AIC) and Bayesian information criterion (BIC) [35, 36, 37], which take into account the predictive power of the model but also the complexity, i.e., the number of non-zero parameters, of the model. Feature selection based on BIC was recently demonstrated to work well for CEs in Ref. 38, 39, 40.

Next, we will consider an example of a simple linear problem with 100 features in order to demonstrate how some of the above mentioned feature selection algorithms work. Training data are generated from a reference linear model, containing only 10 non-zero parameters, with the addition of noise. The parameters obtained from various feature selection methods are shown in Fig. 3.4 using 120 training samples. OLS produces a very noisy parameter vector and fails to reproduce the reference parameters. LASSO and RFE, on the other hand, manage to select the important parameters

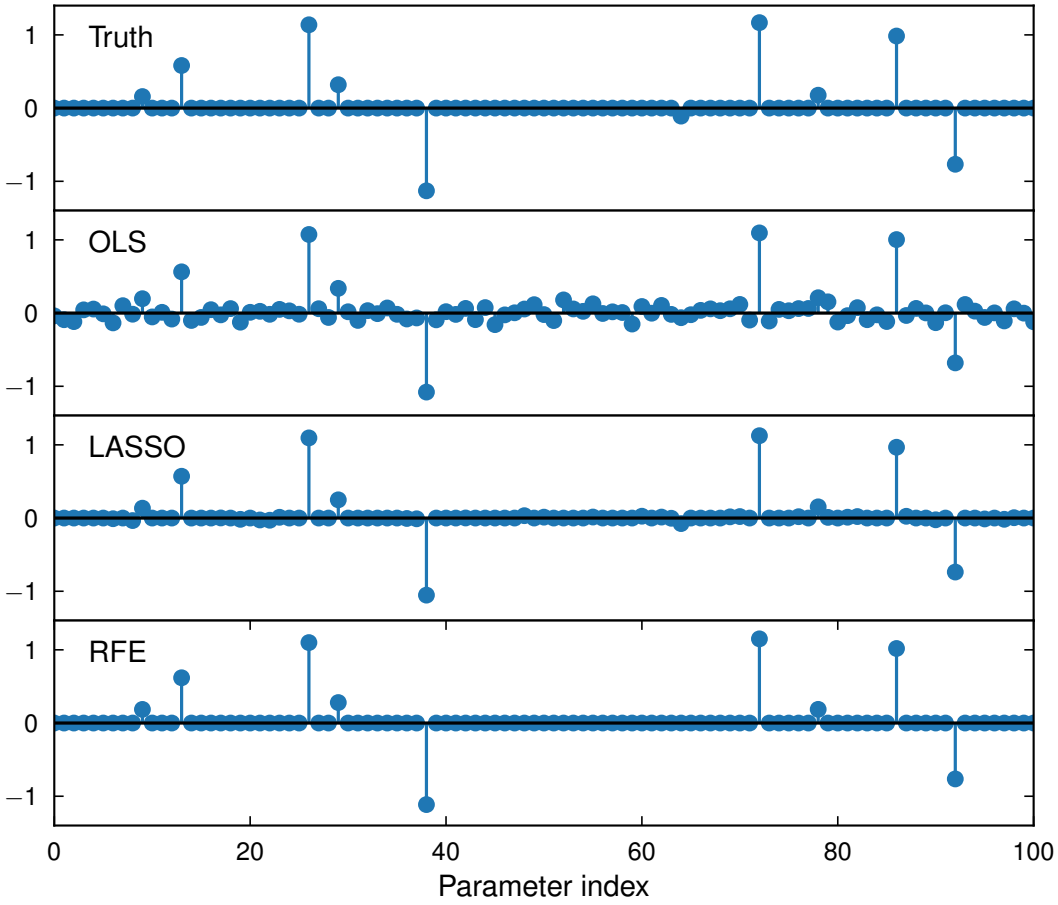

Figure 3.4: Example of parameters obtained using different feature selection methods. Here, a linear problem with 100 features and 120 training samples generated from the true model plus noise is used.

and reproduce the reference parameters rather well. RFE can be used in combination with any linear regression method, although OLS, which is also used here, is the most common. Here, CV analysis was used in order to find the suitable hyperparameters for both LASSO and RFE.

The data and associated scripts for the examples presented in Fig. 3.2, Fig. 3.3 and Fig. 3.4 are available online [41]. It should be noted that the quantitative behavior for these examples changes with different random samples, levels of noise and so on, but the overall qualitative behavior remains the same.

3.4 Monte Carlo simulations

Once a CE has been constructed for the total energy of the system, it can be used to sample various thermodynamic properties and averages. The thermodynamic average for a property A is given by

$$\langle A \rangle = \sum_{\boldsymbol{\sigma}} P(\boldsymbol{\sigma}) A(\boldsymbol{\sigma}), \tag{3.12}$$

where $P(\boldsymbol{\sigma})$ is the probability to observe configuration $\boldsymbol{\sigma}$ and $A(\boldsymbol{\sigma})$ the value of the corresponding property. The probability to observe a configuration requires knowledge of the full partition function, Z, and thus makes $P(\boldsymbol{\sigma})$ difficult to evaluate. This problem is commonly solved using MC simulations with the Metropolis–Hastings algorithm [42], which uses the relative probabilities of two configurations which can be evaluated much more easily.

The MC simulation starts with some initial configuration $\boldsymbol{\sigma}_0$. Next, a (usually small) change to $\boldsymbol{\sigma}_0$ is introduced, generating a trial state $\boldsymbol{\sigma}_t$, which is either accepted or rejected based on the relative probability $P(\boldsymbol{\sigma}_t)/P(\boldsymbol{\sigma}_0)$. This procedure is repeated many times and the MC simulation generates a trajectory of configurations, $\left[\boldsymbol{\sigma}_0, \boldsymbol{\sigma}_1, \ldots \boldsymbol{\sigma}_n\right]$, which corresponds to configurations drawn from $P(\boldsymbol{\sigma})$ if n is large enough. Thermodynamic averages can therefore be calculated as

$$\langle A \rangle = \sum_{\boldsymbol{\sigma} \in \mathrm{MC}} A(\boldsymbol{\sigma}), \tag{3.13}$$

where the summation runs over the configurations in the MC trajectory [21].

For the sake of simplicity, we will here only consider the energy of each configuration in the MC sampling, neglecting the vibrational free energy (see Eq. (2.15)). But if the vibrational free energy (or other free energy contributions) were known for each configuration, then it could straightforwardly be included in the MC simulations according to Eq. (2.15)

3.4.1 Canonical Ensemble

In the canonical ensemble the number of atoms, volume and temperature (NVT) are kept fixed, as discussed in Sect. 2.1.2. In a multicomponent system, the number of atoms, N_α is fixed for each atom type α. The MC simulation is carried out by first occupying a supercell with the desired number of atoms of each species. Then, trial states are generated by swapping the occupation of two sites, which are accepted with probability

$$P = \min\left(1, \mathrm{e}^{-\beta \Delta U}\right), \tag{3.14}$$

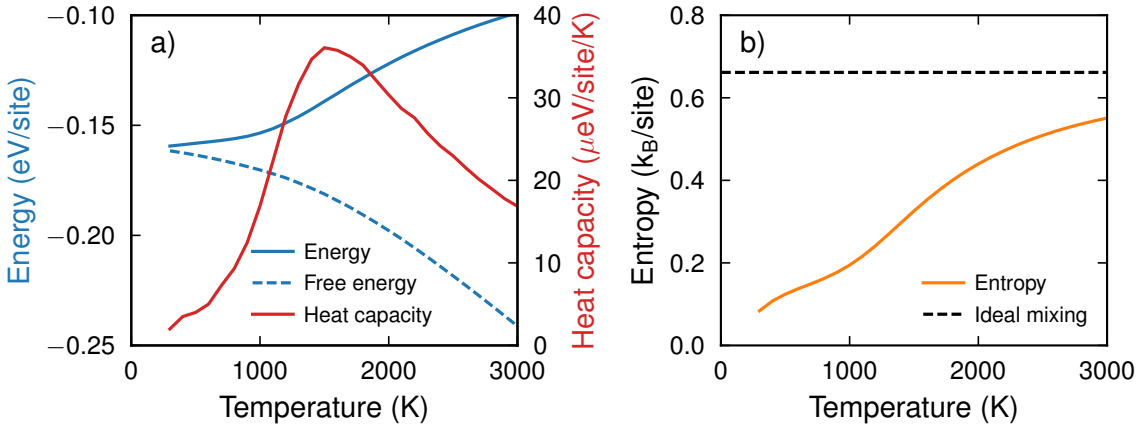

Figure 3.5: Results from MC simulations in the canonical ensemble for the interface system k_4 from Paper VI with a vacancy concentration of 60%. a) Energy, free energy and heat capacity as a function of temperature. c) Entropy as a function of temperature, where the dashed line corresponds to the ideal mixing limit.

where ΔU is the change in energy due to the swap. This will generate configurations according to the probability distribution $e^{-\beta U(\sigma)}/Z_{NVT}$.

The Helmholtz free energy of a system, $F(\{N_\alpha\}, V, T)$, can be calculated via integration using MC simulations in the canonical ensemble. First, we write the free energy in terms of energy and entropy as

$$F(T) = U(T) - TS(T). \tag{3.15}$$

Then the energy, $U(T)$, and the heat capacity, $C_V(T)$, (see Eq. (2.5)) are calculated as thermodynamic averages using MC simulations at various temperatures. The entropy, $S(T)$, can be obtained by integrating the heat capacity over temperature via

$$S(T) = S(\infty) + \int_\infty^T \frac{1}{T} C_V(T) \mathrm{d}T, \tag{3.16}$$

where $S(\infty)$ is the mixing entropy for an ideal mixture. This free energy sampling approach is used in Paper VII and has been demonstrated to work well for CEs previously [43].

In Fig. 3.5 an example of the thermodynamic properties (U, F, C_V and S) obtained from MC simulations are shown as a function of temperature for the interface system k_4 from Paper VI with a carbon vacancy concentration of 60%. With decreasing temperature, the entropy approaches zero and consequently energy and free energy start

to coincide. The heat capacity also approaches zero at low temperatures because the ground-state structure becomes dominant in the MC simulation, which leads to a decrease in the variance of the energy. At high temperatures the entropy is approaching the ideal mixing limit as expected.

3.4.2 Grand Canonical Ensemble

In the grand canonical ensemble the chemical potentials, $\{\mu_\alpha\}$, volume and temperature ($\{\mu_\alpha\}VT$) are kept fixed, see Sect. 2.1.4. The system is in equilibrium with reference states with chemical potentials μ_α for each atom type α. In the grand canonical ensemble, a MC trial move consists of either inserting or removing a single atom, accepted with a probability of

$$P = \min\left(1, \mathrm{e}^{-\beta(\Delta U - \sum_\alpha \Delta N_\alpha \mu_\alpha)}\right), \tag{3.17}$$

where ΔN_α is the change in number of atoms for species α during the trial move [42].

In Paper VI MC simulations in the grand canonical ensemble is used in order to sample the canonical free energy $F(N, V, T)$. For demonstration, we consider the interface system k_4 from Paper VI, which comprises a lattice with N_0 sites that either are occupied by carbon atoms or vacancies. We denote the number of carbon atoms as N_C and the vacancy site concentration is defined as $x = (N_0 - N_\mathrm{C})/N_0$. We use the thermodynamic relation

$$\mu_\mathrm{C} = -\frac{1}{N_0}\frac{\partial F(N_\mathrm{C}, V, T)}{\partial x} \tag{3.18}$$

to extract the canonical free energy for the system. Multiple MC simulations are run in the grand canonical ensemble for a range of μ_C values to obtain the average concentration, $\langle x \rangle$, as a function of μ_C. Since this procedure provides the derivative of the free energy as a function of concentration, the canonical free energy can be obtained by integrating Eq. (3.18).

This approach to calculating the canonical free energy is shown in Fig. 3.6 for the interface system k_4 in Paper VI at 2000 K. The vacancy concentration, x, increases when the carbon chemical potential decreases. This is expected as carbon vacancies are more favorable if the carbon reference state has a lower energy. The energy is directly obtained from the MC simulation and the free energy is obtained by integrating Eq. (3.18). The entropy is extracted via $S = \frac{U-F}{T}$. Here, the entropy as a function of vacancy concentration clearly deviates from the ideal mixing limit with a particular strong deviation at $x = 0.167$. At this concentration there is a very strongly bounded ground-state structure and thus almost no configurational entropy is available even at 2000 K. Lastly, the entropy obtained through simulations in the canonical ensemble at $x = 0.6$, see Fig. 3.5, is shown as a red circle, demonstrating that the entropy, and consequently also the free energy, are in good agreement between the two methods.

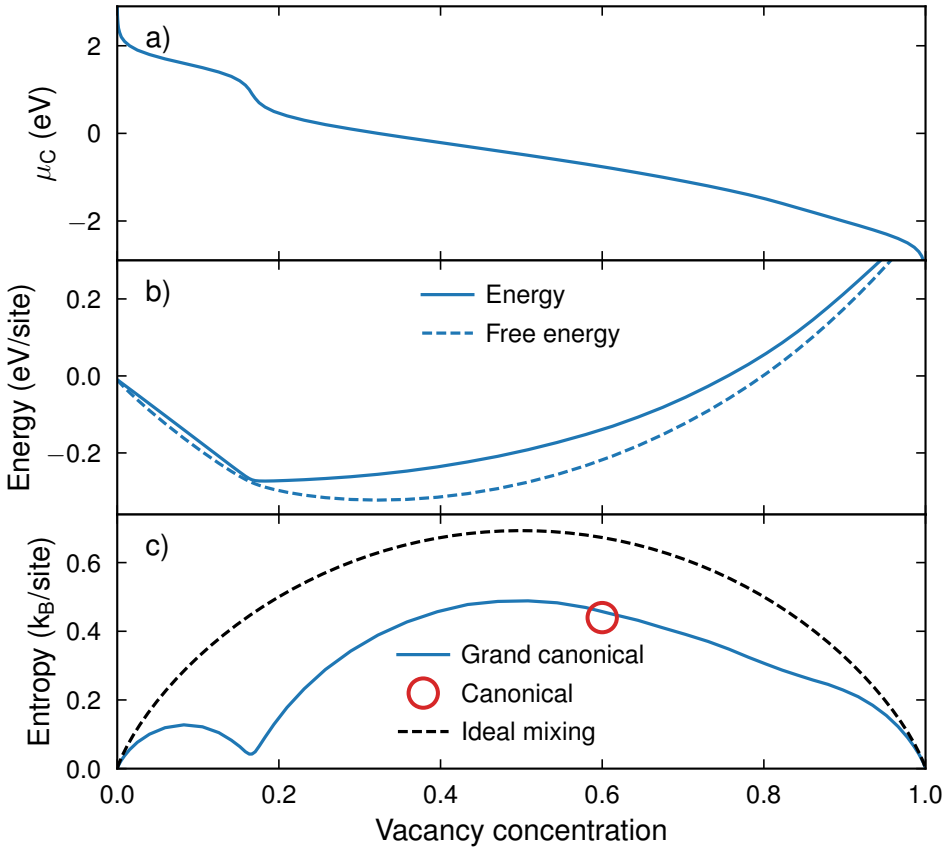

Figure 3.6: Results from MC simulations in the grand canonical ensemble for the interface system k_4 from Paper VI at 2000 K. a) The chemical potential of carbon, μ_C, as a function of the averaged vacancy concentration $\langle x \rangle$. b) The mixing energy and the mixing free energy. c) The mixing entropy as function of vacancy concentration. Here, the red circle indicates the corresponding entropy obtained in the canonical ensemble (see Fig. 3.5), and the dashed line corresponds to ideal mixing entropy.

4

Force constant models

The vibrational motion in a solid is fundamental for understanding many of its properties. Force constants are a way to model the vibrational motion and vibrational properties of a system. Force constant models, similarly to CEs, are also based on a lattice but describe the potential energy associated with displacements, $U(\boldsymbol{u})$, for a specific configuration.

4.1 Formalism

The potential energy for a specific configuration, $U(\boldsymbol{u})$, can be expressed as a Taylor expansion

$$U = U_0 + \Phi_i^\alpha u_i^\alpha + \frac{1}{2}\Phi_{ij}^{\alpha\beta} u_i^\alpha u_j^\beta + \frac{1}{3!}\Phi_{ijk}^{\alpha\beta\gamma} u_i^\alpha u_j^\beta u_k^\gamma + \dots, \tag{4.1}$$

where Φ are the force constants, Latin indices enumerate the atoms, Greek indices enumerate the Cartesian coordinates, and the Einstein summation convention is implied. Here, u describes the displacements from some static positions $\boldsymbol{r}_0$, usually chosen as an ideal lattice for which the first-order term in the expansion vanishes. U_0 corresponds to the energy for the static positions $\boldsymbol{r}_0$. The unknowns in this model are the force constants, where, e.g., second-order force constants are defined as

$$\Phi_{ij}^{\alpha\beta} = \frac{\partial U}{\partial u_i^\alpha u_j^\beta}, \tag{4.2}$$

where the derivative is evaluated at $\boldsymbol{r}_0$, and defined analogously for higher orders.

The number of force constants in the expansion grows rapidly as the number of atoms in the unit cell and the expansion order increase, however, similar to the case

of CEs, symmetries can reduce the number of independent degrees of freedom significantly. One difference compared to CEs is that terms such as Φ_{001} show up in Eq. (4.1), corresponding to a third-order pair interaction. It is often useful to distinguish force constants by both order and the number of atoms (n) involved in the interaction, specially since higher-order pair terms are often important whereas the strength of n-body interactions often decrease rapidly with n.

Force constants can conveniently be obtained using the direct approach [44, 45]. This is commonly done by evaluating the forces for structures where one or only few atoms are displaced. For example, second-order force constants can be obtained via

$$\Phi_{ij}^{\alpha\beta} = \frac{\partial U}{\partial u_i^\alpha u_j^\beta} = -\frac{\partial F_j^\beta}{\partial u_i^\alpha} \approx -\frac{F_j^\beta}{\Delta u_i^\alpha}, \tag{4.3}$$

where F_j^β is the force on atom j in direction β calculated from a structure with a single nonzero displacement Δu_i^α for atom i in direction α. This method works very well and is implemented in many different software packages, e.g., PHONOPY [45] for second-order and PHONO3PY[46], SHENGBTE[47], ALAMODE [48], ALMABTE [49], and AAFLOW [50] for third-order force constants. However, for systems with low symmetry, e.g., defects or interfaces, this method quickly becomes computational intractable due to the large number of supercell calculations required.

4.2 Regression approach

An alternative approach is to extract the force constants via regression. This has been shown to produce accurate force constants [51, 52, 53, 54, 55, 56, 57, 58]. To this end, in Paper I we introduced the python package HIPHIVE for extracting force constants. This approach has the advantages of requiring a much smaller number of DFT calculations and providing better scaling with system size and expansion order. This is possible since the information about the force constants obtained from calculations where only one atom is displaced is quite small compared to the situation when many atoms are displaced simultaneously.

The parametrization of the force constants, including crystal symmetries and sum rules, are explained in detail in Paper I. Using this parametrization and a set of supercells with displacements and forces, the extraction of the independent parameters in the force constants can be cast as a linear problem,

$$\boldsymbol{F} = \boldsymbol{A}\boldsymbol{x}, \tag{4.4}$$

where $\boldsymbol{F}$ are the force components from all supercells, $\boldsymbol{A}$ the design (or sensing) matrix and $\boldsymbol{x}$ denotes the vector of unknown parameters. The number of parameters can be

very large and therefore one commonly limits the order of the force constant expansion and imposes a cutoff, similar to the truncation of a CE. The techniques described in Sect. 3.3 can also be used solve the linear problem for the force constants. The dimensionality of the force-constant problem is often quite large, with up to tens of thousands of rows and columns in $\boldsymbol{A}$, making some of the more computational expensive techniques less feasible to use. In Paper II a comparison of the performance of several different linear regression methods for force constant extraction is carried out. We show that cutoffs, linear regression method and the associated hyperparameters need to be chosen carefully in order to obtain accurate force constants.

4.3 Harmonic approximation

In the harmonic approximation only the second-order force constants are considered. The dynamical properties of a periodic crystal in the harmonic approximation are obtained by constructing the dynamical matrix, $\boldsymbol{D}(\boldsymbol{q})$, for a reciprocal wave vector $\boldsymbol{q}$. Following the notation in [45] it can be calculated via

$$D^{\alpha\beta}_{\kappa,\kappa'} = \sum_{l'} \frac{\Phi^{\alpha\beta}_{0\kappa,l'\kappa'}}{\sqrt{m_\kappa m_{\kappa'}}} \mathrm{e}^{-i\boldsymbol{q}\cdot\left(\boldsymbol{r}_{0\kappa}-\boldsymbol{r}_{l'\kappa'}\right)}, \tag{4.5}$$

where l and κ corresponds to basis atom κ in primitive cell l, $\boldsymbol{r}$ corresponds to the position and m the mass. The harmonic frequencies can then be obtained by solving the eigenvalue problem

$$\boldsymbol{D}(\boldsymbol{q})\boldsymbol{e}_{\boldsymbol{q}j} = \omega^2_{\boldsymbol{q}j}\boldsymbol{e}_{\boldsymbol{q}j}, \tag{4.6}$$

where $\omega_{\boldsymbol{q}j}$ is the harmonic frequency at $\boldsymbol{q}$ with mode index j and $\boldsymbol{e}_{\boldsymbol{q}j}$ the corresponding eigenvector.

If there are N atoms in the system then the harmonic partition function, Z_{har}, can be constructed from the harmonic frequencies as the product of the partition function for $3N$ independent harmonic oscillators. From the harmonic partition function most thermodynamic properties can be derived, including heat capacity, entropy and free energy [59, 60, 45].

The quantum mechanical harmonic free energy, $F_{\mathrm{har}}(T)$, including the kinetic part is given by

$$F_{\mathrm{har}}(T) = \frac{1}{\beta}\sum_i \left[\ln\left(1-\mathrm{e}^{-\beta\hbar\omega_i}\right) + \frac{1}{2}\hbar\omega_i\right], \tag{4.7}$$

where the summation is over all frequencies ω_i with i as a compound index for $\boldsymbol{q}, j$. The last term, $\frac{1}{2}\hbar\omega_i$, corresponds to the zero point energy. The harmonic free energy can be

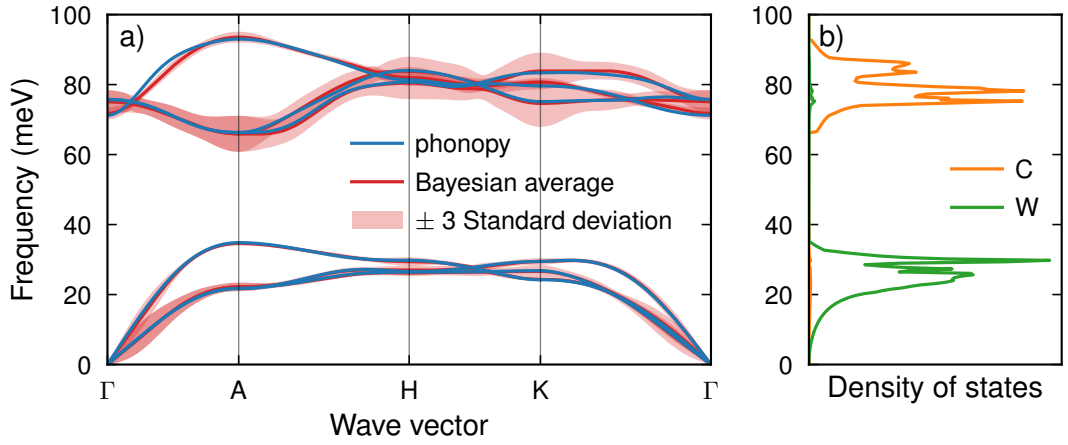

Figure 4.1: a) Phonon dispersion for δ-WC in the harmonic approximation with force constants calculated with PHONOPY and a Bayesian regression approach via HIPHIVE. b) Partial density of states from the force constants obtained using PHONOPY.

written in terms of the harmonic energy and entropy as $F_{\text{har}}(T) = E_{\text{har}}(T) - TS_{\text{har}}(T)$ with

$$E_{\text{har}}(T) = \sum_i \frac{\hbar\omega_i}{e^{\beta\hbar\omega_i} - 1} + \frac{1}{2}\hbar\omega_i \tag{4.8}$$

$$S_{\text{har}}(T) = k_{\text{B}} \sum_i \frac{\beta\hbar\omega_i}{e^{\beta\hbar\omega_i} - 1} - \ln\left(1 - e^{-\beta\hbar\omega_i}\right). \tag{4.9}$$

In the high-temperature limit, $k_{\text{B}}T \gg \hbar\omega$ ($\beta\hbar\omega \to 0$), we obtain the classical result $E_{\text{har}}(T) \to 3Nk_{\text{B}}T$. In this limit the entropy can be approximated as the sum of two terms $S_{\text{har}}(T) = \sum_i S_1(T) + S_2(\omega_i)$, where $S_1(T) = k_{\text{B}}(1 + \ln\left(k_{\text{B}}T\right))$ is frequency independent and $S_2(\omega) = -k_{\text{B}}\ln(\hbar\omega)$ is temperature independent [60]. This means that in the harmonic approximation the free energy difference between two systems in the high temperature limit is given by $\Delta F_{\text{har}} = -T\Delta S_2$, where ΔS_2 is a constant difference in harmonic entropy. This is why defect formation free energies, interface energies and mixing energies in the harmonic approximation show a linear behavior with temperature (see Fig. 4.2 and Fig. 5.1).

Next, the phonons in hexagonal WC are calculated as an example of the harmonic approximation. The phonon dispersion for hexagonal WC is shown in Fig. 4.1a). The force constants are constructed using both the direct approach via PHONOPY and using a Bayesian regression approach. For the latter, one training structure is used with 432 atoms and normal distributed displacements with a standard deviation of 0.01 Å. We use

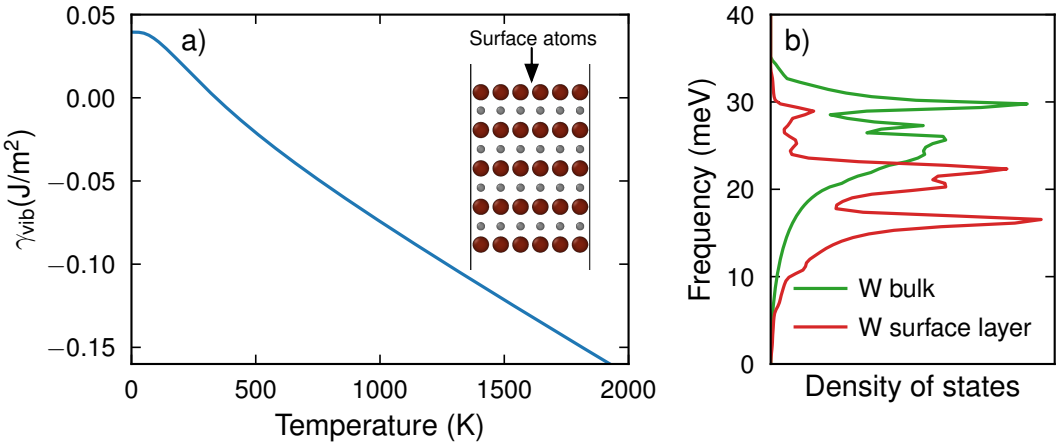

Figure 4.2: a) Vibrational surface free energy, γ_{vib}, of a WC basal surface calculated in the harmonic approximation. The inset shows the atomistic structure of the WC basal surface (W atoms are red and C atoms are grey). b) Partial density of states for W atoms at the surface (red) and in the bulk (green).

the same simple likelihood and priors as in the example shown in Fig. 3.3, with details available online [41]. 200 harmonic models are drawn from their posterior probability distribution and each one is used to calculate the phonon dispersion. The average and standard deviation of the 200 phonon dispersions are shown in Fig. 4.1a). The average dispersion shows good agreement with the PHONOPY dispersion. Further, the partial density of states is shown for the harmonic model from PHONOPY in Fig. 4.1b). Here, we see a clear distinction between the C frequencies and W frequencies. This is caused by the large mass discrepancy between the two, as frequencies $\omega \propto \sqrt{k/m}$ for a force constant k. It is interesting to note that the standard deviation of the frequencies, shown in Fig. 4.1a), is in general larger for the high frequency modes. This is possibly due to the uncertainty in force constants between C and W atoms being similar and thus yielding a larger uncertainty for C frequencies due to their low mass.

Next, we will look at the harmonic free energy for a hexagonal WC basal surface. In general, atoms at a surface are associated with higher (potential) energy compared to the reference bulk phases due to the missing bonds. The cost of creating the surface per area is called the surface free energy and is calculated according to Eq. (2.19). At 0 K the WC basal plane has a surface energy of 3.77 J/m^2 when in equilibrium with bulk WC and graphite [61]. Here, we assume equilibrium with bulk WC and diamond for simplicity's sake. The harmonic approximation is used to calculate the vibrational free energy of the surface system, the bulk WC phase and diamond in order to calculate the

temperature dependency of the surface free energy according to Eq. (2.20). The result is shown in Fig. 4.2a). The diamond phase has higher frequencies than carbon atoms in WC, which leads to a slightly higher zero-point motion energy from the $\frac{1}{2}\hbar\omega$ term in Eq. (4.9) and thus a positive vibrational surface free energy at 0 K is obtained. The W atoms at the surface are missing bonds and are therefore experiencing a softer energy landscape compared to W atoms in bulk WC. This leads to softer frequencies, seen in the density of states Fig. 4.2b), and subsequently a larger vibrational entropy (see Eq. (4.9)), which is the main reason why the surface free energy decreases with temperature. In general, interfaces and defects are associated with softer frequencies and thus interface and defect formation free energies tend to decrease with temperature (see also Fig. 5.1).

For most systems the harmonic approximation is a good approximation for the vibrational free energy, i.e., $F_{\text{vib}} \approx F_{\text{har}}$. However, in the case of strong anharmonicity one can turn to various other approaches to calculate F_{vib}.

4.3.1 Quasi harmonic approximation

Phonon frequencies tend to soften when the volume is increased due to weaker bonds between atoms. Lower frequencies give rise to a larger vibrational entropy and therefore the equilibrium volume tends to increase with temperature, i.e., one observes thermal expansion. This behavior can be captured using the quasi-harmonic approximation (QHA) in which harmonic models are constructed for multiple different volumes [46]. These models are used to obtain the harmonic free energy both as a function of temperature and volume, $F_{\text{har}}(N, V, T)$. This makes it possible to extract Gibbs free energy for a given pressure, P, via Eq. (2.10) as

$$G(N, P, T) = \min_V \left[F_{\text{har}}(N, V, T) + PV \right]. \tag{4.10}$$

The equilibrium volume as a function of temperature, $V_{eq}(T)$, can be found in the same manner via

$$V_{eq}(T) = \operatorname*{argmin}_V \left[F_{\text{har}}(N, V, T) + PV \right]. \tag{4.11}$$

In Paper IV, the QHA is used to describe the free energy of the WC hexagonal bulk phase at $P = 0$. The hexagonal lattice has two lattice parameters a and c. In this case, to find the equilibrium lattice parameters, the minimization is carried out simultaneously with respect to both lattice parameters, i.e.

$$(a_{eq}(T), c_{eq}(T)) = \operatorname*{argmin}_{a,c} F(a, c, T). \tag{4.12}$$

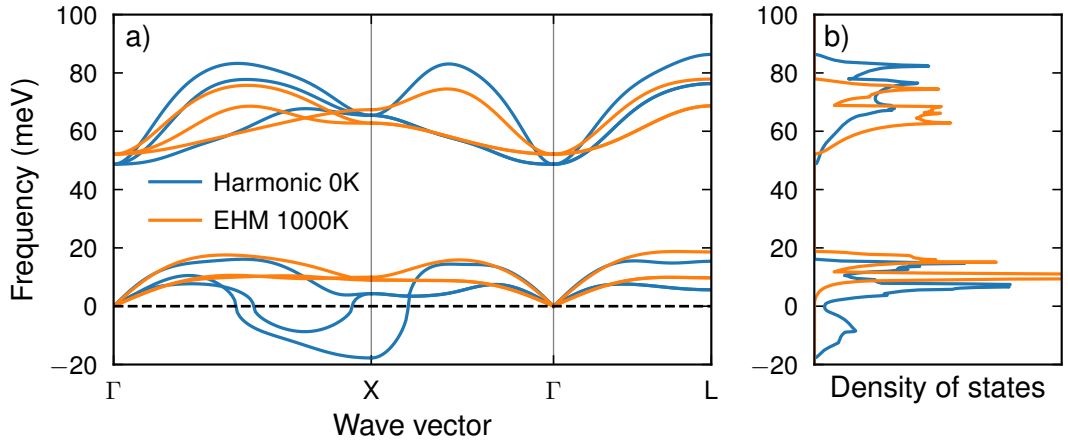

Figure 4.3: a) Phonon dispersion for cubic WC for a regular harmonic model (0 K) and an effective harmonic model (EHM) computed from an ab-initio MD simulation at 1000 K. Here, the same volume is used for the harmonic model and the effective harmonic model. b) Density of states for the two harmonic models.

4.3.2 Effective harmonic models

One of the simpler, yet powerful methods to account for anharmonicity is to construct EHMs from MD simulations [62, 63]. An EHM is a harmonic model which aims to effectively describe an anharmonic system at a specific temperature. This is commonly done by constructing a harmonic model with the regression approach using displacements and forces from a MD simulation, which effectively incorporate anharmonic effects into the harmonic model. This approach of constructing EHMs is commonly referred to as temperature dependent effective potential (TDEP) [53]. Once the EHM is constructed it can be used as a regular harmonic model to predict, e.g., phonon dispersion and thermodynamic properties.

A good example where EHMs are useful is the cubic WC phase which is dynamically unstable at low temperatures but stabilized at higher temperatures. The phonon dispersion for cubic WC is shown in Fig. 4.3 for a regular harmonic model constructed using PHONOPY, corresponding to 0 K, and an EHM at 1000 K. The regular harmonic model has imaginary frequencies, shown as negative, which indicates structural instabilities, whereas in the EHM these modes are stable. The EHM is constructed from an ab-initio MD simulation using the same volume as for the harmonic model, meaning thermal expansion is not taken into account in this example. Thermal expansion can be captured by EHMs by running MD simulations at many volumes and applying Eq. (2.10) as demonstrated in Paper V.

EHMs can also be constructed from self-consistent phonons (SCP). This can be implemented in various different ways [64, 65, 66], which are not further differentiated here. An overview of these methods is given in Ref. 67. A few recent studies have compared the behavior and accuracy of EHMs constructed from SCP and TDEP [68, 69]. Although, it is not clear that one approach is strictly better than the other, one downside with the TDEP approach is that it relies on MD simulations which are often carried out in a classical setting and hence would not sample displacements and forces correctly below the Debye temperature. In a SCP approach, on the other hand, quantum mechanical effects can be incorporated. One big upside of TDEP is the simplicity of the approach and how readily it can be applied to almost any system.

4.3.2.1 Free energy perturbation

Free energy perturbation can be applied in order to improve the free energy accuracy of EHMs [70]. It describes the free energy difference between two Hamiltonians A and B as

$$F_A - F_B = \frac{1}{\beta} \ln \left\langle \mathrm{e}^{-\beta(U_B - U_A)} \right\rangle_A , \tag{4.13}$$

where U_A and U_B is the energy from Hamiltonians A and B, respectively, and $\langle \ldots \rangle_A$ denotes an ensemble average carried out in Hamiltonian A [70]. In the case of EHMs, the EHMs correspond to Hamiltonian B and the reference Hamiltonian (often DFT) to A. Eq. (4.13) provides a correction to the effective harmonic free energy, F_B, and thus gives a better estimate of the free energy of the reference system A, F_A. This correction can conveniently be applied as the EHM is constructed from a MD simulation carried out with Hamiltonian A, which allows the ensemble average in Eq. (4.13) to be evaluated [71]. The free energy perturbation is similar to the correction carried out in Ref. 53 where U_0 from Eq. (4.1) is determined in order to minimize $\langle U_A - U_B \rangle_A$.

4.4 Higher-order models

Next, we will consider the applications of higher-order force constant expansions. Third-order force constants can be used to calculate phonon lifetimes using perturbation theory [59]. Phonon lifetimes can, for example, be used to compute the lattice thermal conductivity via Boltzmann transport theory [46]. Fourth-order force constants can be used to renormalize the harmonic frequencies with SCP [66].

Higher-order force constant models can also be used more directly to describe the potential energy surface. This is demonstrated in Fig. 4.4, where the energy landscape of the imaginary mode of the cubic WC phase at the X point (see Fig. 4.3) is shown. The energy landscape is constructed directly using DFT, the harmonic model, an EHM from 1000 K and a sixth order model. The higher order model is trained from them same data

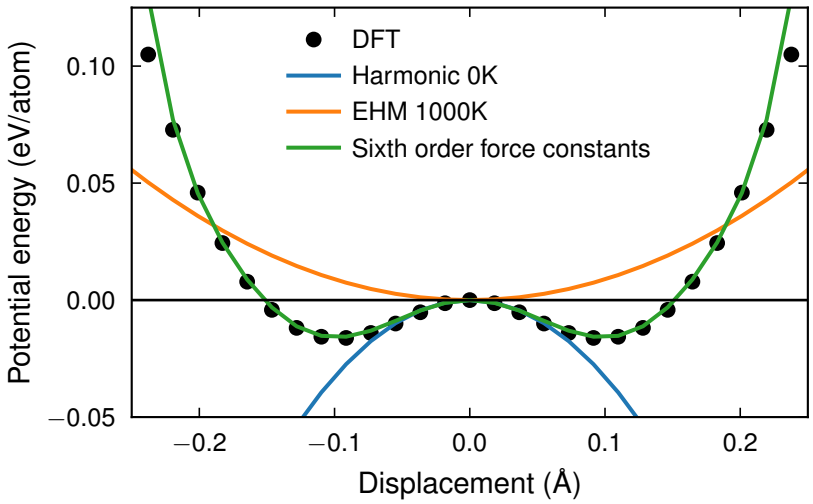

Figure 4.4: Potential energy landscape for the cubic WC phase along the imaginary phonon mode at X, constructed using DFT, an effective harmonic model at 1000 K, a regular harmonic model and a higher order models. The x-axis corresponds to the average displacement of all atoms along the phonon mode.

as the EHM, as well as data along the phonon mode path. This is not meant to be the optimal higher order model for the cubic WC phase but rather illustrate that this type of anharmonic energy landscape can be captured with higher-order models.

Fig. 4.4 also highlights the fact that in the harmonic approximation this mode is unstable and is stabilized with an EHM at 1000 K. The EHM is a better approximation of the energy landscape compared to the harmonic model for large displacements corresponding to 1000 K. However, it is important to note that the EHM is still not a great approximation for this anharmonic mode. This makes combing the EHM with perturbation theory (see subsubsection 4.3.2.1) important in order to obtain an accurate vibrational free energy for strongly anharmonic systems.

Fourth and higher-order models can also be used to run MD simulations from which thermodynamic properties can be extracted [54]. This is demonstrated for a clathrate in Paper II, where the temperature dependence of the phonon spectrum is directly sampled from MD simulations. A problem with this approach is that,MD simulations with higher-order force constant potentials can become unstable with displacements increasing indefinitely. This problem was also noted in recent work, Ref. 55, where inclusion of short-ranged strongly anharmonic pair potentials was used to stabilize the potential. In our experience, regularization and inclusion of training structures with large displacements can stabilize higher-order force constant models without additional

stabilizing terms. At some point, though, the anharmonic effects and tendencies for diffusion become too large to model with force constants and one must employ other methods in order to model the potential energy surface.

5

Interatomic potentials

Interatomic potentials are in general more flexible than CEs and force constant models. The potential energy, U, can be written as

$$U = U(\boldsymbol{r}_1, \ldots, \boldsymbol{r}_i, \ldots, \boldsymbol{r}_N), \tag{5.1}$$

where $\boldsymbol{r}_i$ is the position of atom i and N the total number of atoms. Implied here is also the knowledge about the atom types. Interatomic potentials are not limited to solids or a fixed lattice but in principle also applicable to liquid and gas phases as well as molecules.

5.1 Pair potentials

One of the simplest form of an interatomic potential is a pair potential, in which the potential energy is only dependent on the interatomic distances in the system. One of the more well known pair potentials is the Lennard-Jones potential [72], which can be written as

$$U = \sum_{i<j} 4\varepsilon \left[\left(\frac{\sigma}{r_{ij}} \right)^{12} - \left(\frac{\sigma}{r_{ij}} \right)^{6} \right], \tag{5.2}$$

where r_{ij} is the distance between atom i and j. ε and σ are the free parameters of the potential which controls the energy and length scale, respectively. Pair potentials, such as the Lennard-Jones potential, work well for simple systems, e.g. noble gases and ionic systems, but tend to fail for e.g. metallic or covalent bonding.

5.2 Embedded atom method potentials

The functional form of the embedded atom method (EAM) consists of a pair potential and an additional term that represents the energy associated with embedding an atom in the electron density provided by the surrounding atoms. This approach has been developed to model electronic many-body effects in metallic systems. The functional form of an EAM is usually written as

$$U = \sum_{i<j} \phi(r_{ij}) + \sum_i F\left(\sum_{j\neq i} \rho(r_{ij})\right), \tag{5.3}$$

where $\phi(r_{ij})$ is the pair potential, F the embedding function and ρ_i the density function. ϕ, F and ρ are commonly determined by choosing sufficiently flexible functional forms, the parameters of which are then fitted to reference data, e.g., from experiment and DFT calculations. There exist multiple variants of this potential form known as EAM [73], effective medium theory (EMT) [74] and Finnis-Sinclair) [75]. While the EAM scheme has been very successful for metals, the potential form does not describe directional bonding very well, which is crucial for covalent systems such as WC.

5.3 Analytical bond order potentials

In order to deal with strong directional bonding one has to add explicit three-body terms to the interatomic potential. An example of this is the ABOP [76, 77, 78] form

$$U = \sum_{i<j} f^c(r_{ij}) \left(V^R(r_{ij}) - b_{ij} V^A(r_{ij})\right), \tag{5.4}$$

where V^R and V^A are respectively repulsive and attractive Morse-like pair potentials and f^c is a cutoff function, which smoothly scales energy and forces to zero as the interatomic distance, r_{ij}, increases. Here, b_{ij} is the bond-order term, which involves explicit three-body terms.

In Paper IV, we employ an ABOP for calculating interface free energies in the WC–Co system at finite temperatures. This potential was constructed using parameters for C–C interactions from Ref. 78, W–W and W–C interactions from Ref. 79 as well as Co–Co, C–Co, and W–Co interactions from Ref. 80.

5.4 Molecular dynamics simulations

Thermodynamic sampling using interatomic potentials can often be carried out effectively via MD simulations [21]. In MD simulations the atomic positions and velocities

are evolved in time using classical mechanics and an interatomic potential according to

$$m_i \frac{\partial^2 \boldsymbol{r}_i(t)}{\partial t^2} = \boldsymbol{f}_i(t) \tag{5.5}$$

$$\frac{\partial \boldsymbol{r}_i(t)}{\partial t} = \boldsymbol{v}_i(t), \tag{5.6}$$

where m_i, $\boldsymbol{r}_i(t)$, $\boldsymbol{v}_i(t)$ and $\boldsymbol{f}_i(t)$ are respectively the mass, position, velocity and force associated with atom i at time t. The force acting on an atom $\boldsymbol{f}_i(t)$ is computed from the interatomic potential as

$$\boldsymbol{f}_i(t) = -\frac{\partial U(\boldsymbol{r}_1(t), \ldots, \boldsymbol{r}_N(t))}{\partial \boldsymbol{r}_i}. \tag{5.7}$$

The integration of the equation of motion, Eq. (5.6), is carried out numerically for discrete times, often using the Verlet algorithm [81]. This will result in sampling in the microcanonical ensemble (NVE) since the system is isolated and, thus, the total energy in the system is conserved. The temperature, using the equipartition theorem, is given by

$$T = \frac{2}{3k_B} \left\langle \frac{1}{2} m |\boldsymbol{v}|^2 \right\rangle, \tag{5.8}$$

where $\langle \ldots \rangle$ denotes the ensemble average of the kinetic energy per atom [21]. If the system is ergodic, ensemble averages can be replaced by time averages, which are easily evaluated from MD simulations. For example, for a quantity A the thermodynamic average can be computed by

$$\langle A \rangle = \frac{1}{N_{\text{steps}}} \sum_{i}^{N_{\text{steps}}} A(t_i), \tag{5.9}$$

where the sum runs over the MD trajectory, t_i is the time at the i-th timestep and and N_{steps} is the total number of timesteps.

5.4.1 Thermodynamic integration

A very effective way of calculating free energies using MD simulations is thermodynamic integration between two Hamiltonians, H_A and H_B. Here, A represent a system for which the free energy is obtained and B a system for which the free energy is known. Constructing a Hamiltonian as

$$H(\lambda) = (1 - \lambda) H_A + \lambda H_B \tag{5.10}$$

allows for the free energy difference between A and B to be computed via

$$F_B - F_A = \int_0^1 \left\langle \frac{\mathrm{d}H(\lambda)}{\mathrm{d}\lambda} \right\rangle_H \mathrm{d}\lambda, \tag{5.11}$$

where the integration is carried out over the Kirkwood coupling parameter λ [82]. Here, the ensemble average $\langle \ldots \rangle_H$ should be carried out using the full Hamiltonian H. The choice of linear mixing between H_A and H_B in Eq. (5.10) is not required but makes the integral in Eq. (5.11) easy to evaluate. This free energy calculation method is commonly referred to as λ-integration.

The Hamiltonian H_B needs to be chosen such that its free energy is known. One common choice for B is an Einstein solid, which is sometimes referred to as the Frenkel-Ladd method [83]. In an Einstein solid the atoms oscillate around their lattice points as independent classical harmonic oscillators with frequency ω_E. The classical free energy of an Einstein solid, F_E, is

$$F_E = 3Nk_BT \ln\left(\frac{\hbar\omega_E}{k_BT}\right). \tag{5.12}$$

When doing this type of free energy integration it is important that the two Hamiltonians in questions are not too dissimilar as this will make convergence of the method very slow. In practice, the Einstein frequency is therefore usually chosen to, e.g., reproduce the mean square displacement for system A for the desired temperature. For a multi-component system with large mass discrepancy, such as WC, one can also assign different Einstein frequencies for the different atomic species. The integration can be done either via equilibrium sampling at a few carefully chosen λ values or by changing λ continuously throughout the simulation [84].

Additionally, if the free energy is known at a single temperature, T_1, it can be found for other temperatures via temperature integration. This is done via

$$\frac{F(T_2)}{T_2} = \frac{F(T_1)}{T_1} - \int_{T_1}^{T_2} \frac{U}{T^2}\mathrm{d}T, \tag{5.13}$$

and hence only requires knowledge of the temperature dependence of the internal energy, $U(T)$ [85]. This is essentially the same approach as described in Eq. (3.16) but here written for the free energy rather than for the entropy.

5.5 Free energy example of vacancy in BCC Ta

Next, some of the free energy calculation methods are used to compute the vacancy formation energy, $\Delta G_\mathrm{f}^\mathrm{vac}(T)$, up to the melting point in body-centered cubic (BCC) Ta.

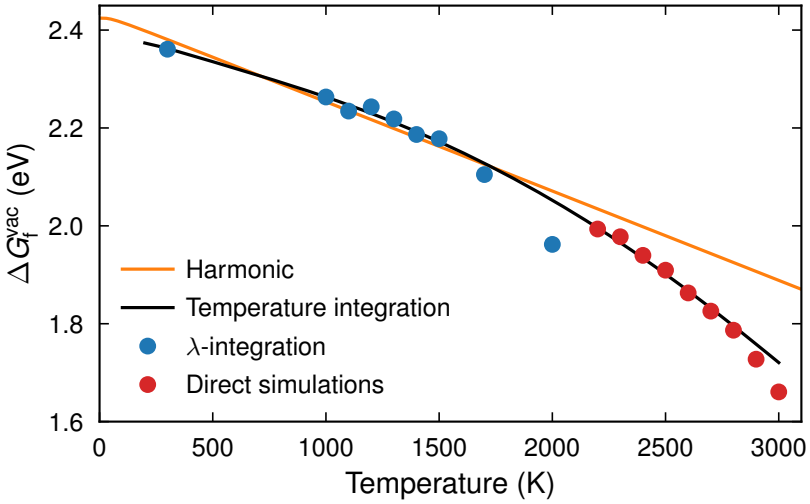

Figure 5.1: Vacancy formation energy, $\Delta G_f^{vac}(T)$, in BCC-Ta as a function of temperature calculated using the harmonic approximation, λ-integration, temperature integration and "direct" simulations. The direct simulations are carried out for a larger system with open surfaces, and the vacancy concentration is directly measured in the bulk region of the system.

This is done by computing free energy of the bulk system and a system with a single vacancy. Here, an EAM potential is used [86], which has a melting point of about 3050 K.

The resulting formation energy is shown in Fig. 5.1. Here, thermal expansion of the bulk and vacancy system is taken into account for all methods except for the harmonic approximation. The formation energy at 0 K is about 2.4 eV. In the harmonic approximation $\Delta G_f^{vac}(T)$ decreases linearly with temperature, as expected see Sect. 4.3.

λ-integration is carried out using an Einstein solid as reference Hamiltonian, via Eq. (5.11). For temperatures above 1500 K, the vacancy starts to migrate in the MD simulations. Although migration is rare at 1500 K, when diffusion occurs the λ-integration method fails since it relies on fixed reference positions. To overcome this problem temperature integration, Eq. (5.13), is employed. Here, the free energy obtained using λ-integration at 300 K is used as the known free energy F_1 in Eq. (5.13). In this case, diffusion is not a problem since temperature integration only requires knowledge of the temperature-dependent internal energy, $U(T)$, of the system, and the vacancy formation energy can be obtained as a function of temperature up to the melting point.

Lastly, the vacancy concentration is measured directly from MD simulation of a large system with open surfaces in the z-direction direction. This approach relies on the fact

that vacancies can spontaneously form at the surfaces and migrate into the bulk region of the system [87, 88]. Therefore, an equilibrium number of vacancies is obtained in the bulk region, and the vacancy formation energy is obtained by inverting the expression from the dilute limit, Eq. (2.18).

The free energy example shown in Fig. 5.1 demonstrates the accuracy, advantages and disadvantages of different free energy calculations methods. The harmonic approximation is easy to employ and does not require any large-scale simulations, however, its accuracy decreases as temperature increases. λ-integration accounts for anharmonicity, but in this system does not yield any significant improvements compared to harmonic approximation. Additionally, the λ-integration method requires the system to stay in a well defined configuration (see Fig. 2.2) without diffusion. Temperature integration relies on knowledge of the free energy at some temperature, but can then be used to find the accurate free energy of the system at any temperature even if the system starts rapidly moving between configurations (see Fig. 2.2). The vacancy formation energy close to the melting point calculated with temperature integration agrees very well with values obtained from direct measurements of the vacancy concentration. Below 2000 K, vacancy migration is not fast enough to generate an equilibrium vacancy concentration during the timescales considered in the direct measurement simulations. This means that movement between different configurations (see Fig. 2.2) is not fast enough to allow the MD simulations to sufficiently sample the energy landscape.

6

Cemented Carbides

6.1 General

Cemented carbides, also known as hardmetals, combine both hardness, i.e. the ability to resist plastic deformation, and toughness, i.e. the ability to absorb energy and deform plastically without fracturing [8]. These are two competing properties, meaning as one increases the other tends to decrease. For example, diamond is a very hard material but also brittle (low toughness) and shatters easily. Another example would be aluminum, which is not a hard material but instead can easily be bent and shaped without fracturing. The excellent mechanical properties of cemented carbides make them ideal for usage in diverse applications including high-speed machining of steels and in wear-resistance tools [12, 89].

The most commonly used cemented carbide is WC–Co, which is the material studied in this thesis. The cemented carbide microstructure consists of WC grains forming a continuous skeleton embedded in a Co binder phase. A typical WC–Co microstructure is shown in Fig. 6.1. The WC grains provide hardness whereas the Co binder phase adds toughness to the material [90].

6.2 Manufacturing

The WC–Co cemented carbide is manufactured from powders of carbide and binder. First, the powders are mixed and milled in order to create a uniform mixture and to reduce the carbide grain size. The milled powders are then pressed to a desired tool shape and finally sintered [90]. The goal of the sintering is to densify the cemented carbide by eliminating pores, obtain strong inter-grain bonds and achieve a desired microstructure. The sintering is often done in several steps, usually reaching temperatures above

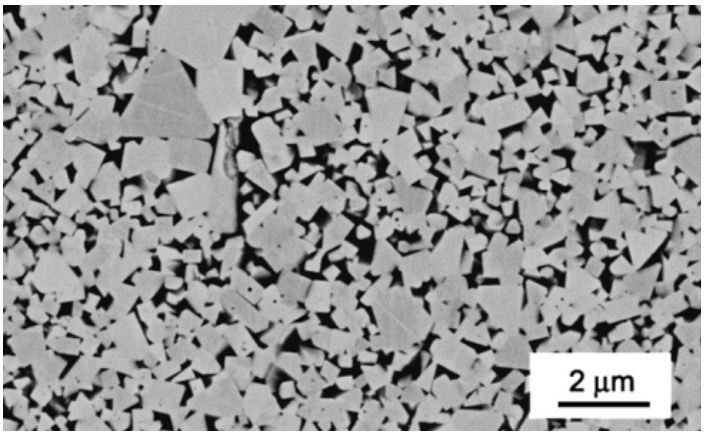

Figure 6.1: Scanning electron microscopy micrograph showing the typical microstructure of WC–Co with 12 at% Co, from Ref. 13. Here the grey regions indicate the WC grains, and the black region the Co-rich binder.

1300 °C for which the Co-rich binder melts. This separates the sintering process into solid-state sintering and liquid-phase sintering.

One important aspect of manufacturing is the carbon content which has a significant impact on the mechanical properties. A cross section of the phase diagram of W–C–Co for a system with 10 wt% Co as a function of carbon content and temperature is shown in figure Fig. 6.2. When manufacturing, it is desirable to be in the so-called carbon window where only WC and Co are stable in order to avoid the formation of either the so-called η-phases or graphite. η-phases are complex carbides that occur if the carbon content is too low. At low temperatures the η_{12}-phase ($M_{12}C$) will form, whereas at temperatures above 1150 °C the η_6-phase (M_6C) will form [91]. Since the η-phases are brittle, they are detrimental to the mechanical properties of the cemented carbide. If on the other hand the carbon content is too high graphite will form which reduces the strength of the cemented carbide.

6.3 WC crystal structure

The ground-state WC bulk phase in cemented carbides is the hexagonal phase, δ-WC. There exist, however, multiple other WC phases, specifically at high temperatures and low carbon content [92]. One of these is the cubic phase, γ-WC, phase which has a rocksalt crystal structure, which is the ground-state structure for other carbides such as VC [93] and TiC [42]. γ-WC becomes thermodynamically stable at about 3000 K, which is very close to the melting point of WC. Additionally, the cubic phase is also stable for a substoichiometric carbon composition, WC_x, which is achieved via incorporation of

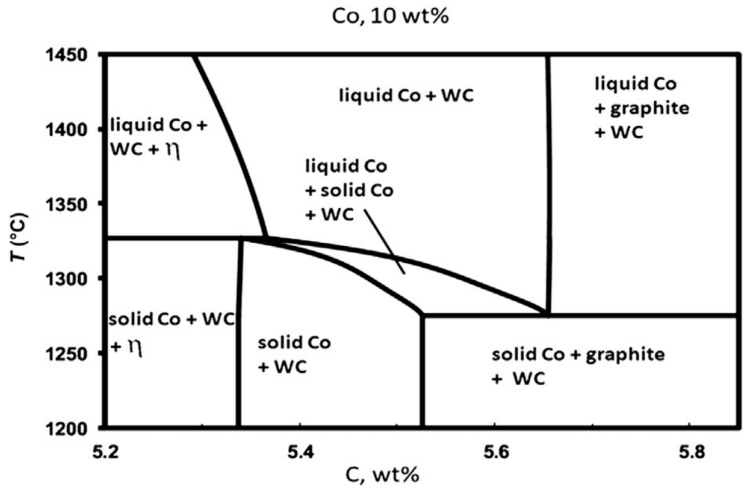

Figure 6.2: Cross section of phase diagram of W–C–Co system for 10 wt% Co as a function of carbon content and temperature, from Ref. 90.

carbon vacancies [92]. The hexagonal phase contains almost no carbon vacancies even close to the melting point. In Paper V the thermodynamics and free energies of these two WC phases (δ-WC and γ-WC) were studied in detail.

6.4 Microstructure

The microstructure of cemented carbides, shown in Fig. 6.1, consists of WC grains forming a continuous skeleton in the Co-rich binder phase. The equilibrium shape of WC grains are truncated triangular prisms because this shape yields the lowest overall interface energy [94]. Typically, the WC grain size ranges from 200 nm to 10 μm [90]. The evolution of the microstructure during sintering is driven by the reduction of the total interface free energy in the system, which can be done via reducing the interface area and reorienting grains to find favorable interface orientations. Understanding the interfacial free energies both for solid-state and liquid-phase sintering conditions can, thus, help with understanding and predicting the microstructure.

The mechanical properties of the cemented carbide WC–Co are closely connected to its microstructure [13]. Specifically, the average size of the WC grains has a significant impact on the mechanical properties, where smaller grains yield a harder material. A finer microstructure also results in a decrease in toughness due to the inverse proportionality between hardness and toughness [13, 95]. Controlling the microstructure is thus important in order to be able to design a material with desirable mechanical properties. Therefore, an important research topic in the cemented carbides industry is to

understand the atomistic mechanisms that dictate grain growth during sintering.

6.5 Grain growth

Grain growth is driven by the reduction in the total interface free energy in the system. Few large grains have less interface area than many smaller grains, which gives rise to a driving force for grain growth. This can happen via so-called Ostwald ripening, where smaller grains dissolve while their components, after diffusion through the binder phase, reprecipitate on larger grains [96]. The grain growth in cemented carbides mainly occurs during liquid-phase sintering [97]. In WC–Co the measured grain growth rate is slow compared to W and C diffusion in the liquid binder phase, and therefore WC grain growth could be limited by either dissolution or precipitation. As the dissolution process has, however, been shown to occur rapidly [98], precipitation is the rate limiting step in the WC grain growth process [99, 100, 101].

For growth of faceted grains the precipitation step is commonly divided into two processes: nucleation and lateral growth. First, a new atomic layer has to nucleate by atoms attaching to the surface [102, 103]. Subsequently, the nucleus grows laterally until a complete atomic layer has been formed [100, 104]. The precipitation step is thus limited either via the nucleation event or the lateral growth.

Grain growth in WC–Co has recently been modeled via simulations in Ref. 105. In this work the rate limiting process was found to be dependent on the grain size. For smaller grains the growth was limited by nucleation of atomic layers and for larger grains the growth was limited by lateral growth.

6.5.1 Carbon content

When manufacturing cemented carbides the carbon content can be controlled and varied. The WC grain growth behavior has been shown to vary with the amount of carbon. For WC–Co materials in equilibrium with η phases (W-rich materials) smaller WC grains are obtained compared to WC–Co materials in equilibrium with graphite (C-rich materials) [106, 107, 108, 109, 110, 101].

Borgh et al. [110] studied the grain size distribution in five WC–Co materials with carbon content varying from W-rich to C-rich conditions. They denoted these materials WC–Co–eta, WC–Co–(eta lim), WC–Co, WC–Co–(graphite lim) and WC–Co-graphite. The grain size (equivalent circle diameter) distribution was measured via electron backscatter diffraction (EBSD) in the five materials. They report the full grain size distribution (see their Fig. 3) as well as distribution parameters D10, D50, D90. D50 is the diameter for which the area of all grains smaller than D50 corresponds to 50% of the total area, and can be thought of as an average grain size. In Table 6.1 the composition of their materials and measured grain size parameters are reproduced. From the

	WC–Co–eta	WC–Co–(eta lim)	WC–Co	WC–Co–(gra lim)	WC–Co-gra
C (at%)	39.85	40.35	40.80	41.12	42.00
W (at%)	42.26	41.76	41.31	40.99	40.11
D10 (μm)	0.769	0.808	0.913	0.951	0.989
D50 (μm)	1.507	1.553	1.733	1.726	1.796
D90 (μm)	2.634	2.732	3.137	3.049	3.284

Table 6.1: Materials studied by Borgh et al. and their corresponding grain size measurements [110], values are from their Tables 1 and 2. All materials had a Co concentration of 17.89 at%. Here, graphite is shortened to gra.

D50 values one can see that the grain size does not continuously vary with C content. Instead, WC–Co–eta and WC–Co–(eta lim) have roughly the same grain size distribution, and WC–Co, WC–Co–(graphite lim) and WC–Co-graphite have similar grain size distributions.

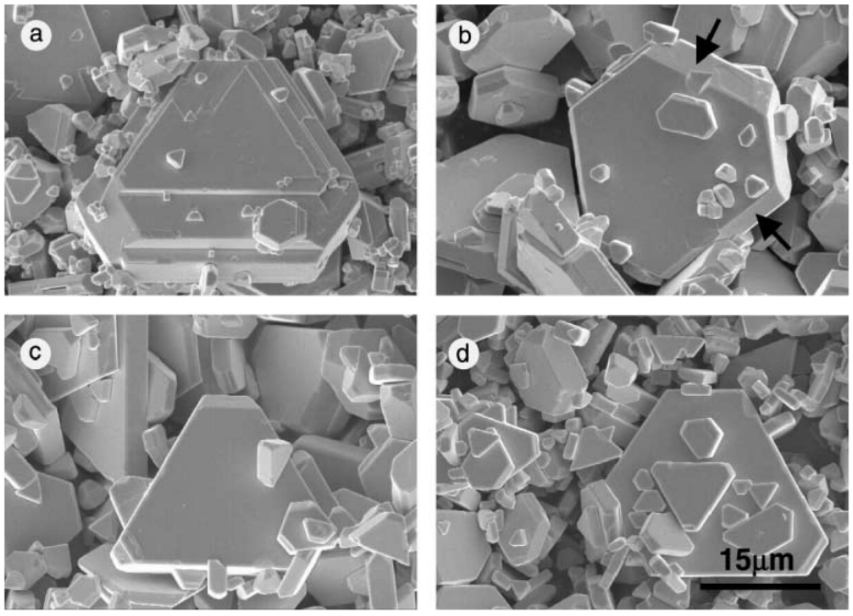

Figure 6.3: Image of WC grains in four different WC–Co materials with 30 wt% Co, from Ref. 111. The materials, a,b,c,d have a carbon content beyond stoichiometric WC of 0.1 wt%, 0.3 wt%, 0.7 wt% and 1.0 wt%, respectively.

This type of grain size variation with respect to carbon content is also found in the work by Wang et al. [112], who analyzed three materials: WC–Co-C, WC–Co, and WC–Co-W. The first corresponds to a C-rich material, the second one to a material

inside the carbon window and the third one to a W-rich material. They report that the grain size is similar in WC–Co and WC–Co-C, whereas smaller grains are observed in the WC–Co-W material. This is specifically clear in their Fig. 4., where the grain size distribution is shown after 2 hours of sintering.

Additionally, WC grains in C-rich materials are often perfectly faceted, whereas steps and terraces are observed on the WC grains in W-rich materials [112, 111, 110, 101]. A clear image of these type of steps are shown in Fig. 6.3a, which has been redrawn from Ref. 111. Here, the material in a is in equilibrium with η phase, b is inside the carbon window while c and d are in equilibrium with free carbon.

Roulon et al. [101] argue that the presence of steps in W-rich material is an indication that lateral growth is the rate limiting process, whereas in C-rich materials no steps are observed and thus 2D nucleation would be limiting. If lateral growth is fast compared to the nucleation, then one expects perfectly faceted grains. However, if lateral growth is instead slow compared to the nucleation, then multiple nuclei may be present at a given time and steps could form. These two types of growth behavior are schematically illustrated in Figs. 5 and 6 in Paper VI. Further, in Paper VI we suggest a possible explanation to why lateral growth would be slow in W-rich materials, namely due to the formation of thin cubic films at WC–Co phase boundaries.

6.5.2 Grain growth inhibitors

The grain growth rate can be inhibited via addition of so-called grain growth inhibitors [114, 115, 113]. The most common grain growth inhibitors are transition metals such as V, Ti, Cr, Ta, Mo, and Nb [10], where V is the most potent [115]. Fig. 6.4 shows the grain size for WC–Co materials (20 wt% Co) with varying amounts of added dopants [113]. For Hf and Zr almost no inhibition is observed, while for other dopants (V, Mo, Cr, Nb, Ta, Ti) the inhibition effect increases with doping level until a plateau is reached. The point at which these plateaus are reached is likely related to the solubility limit for the dopants in Co.

The mechanism behind grain growth inhibition is a widely discussed topic in the cemented carbide community and not yet fully understood. It is possible that inhibitors in some way interfere with the grain growth processes at the interfaces, i.e,. nucleation and lateral growth [115, 116, 117, 118, 113].

These dopants are frequently observed to segregate to the phase boundaries between WC and Co. Segregation to the WC–WC grain boundaries is also observed, together with Co segregation [119]. The segregation to the phase boundaries is often identified as thin cubic films, with rocksalt type crystal structure and composition (M,W)C_x. This type of interfacial structures are commonly referred to as complexions [120]. In general, the cubic films most often form on the WC basal plane in contact with Co, but films have also been observed on the prismatic WC planes [121].

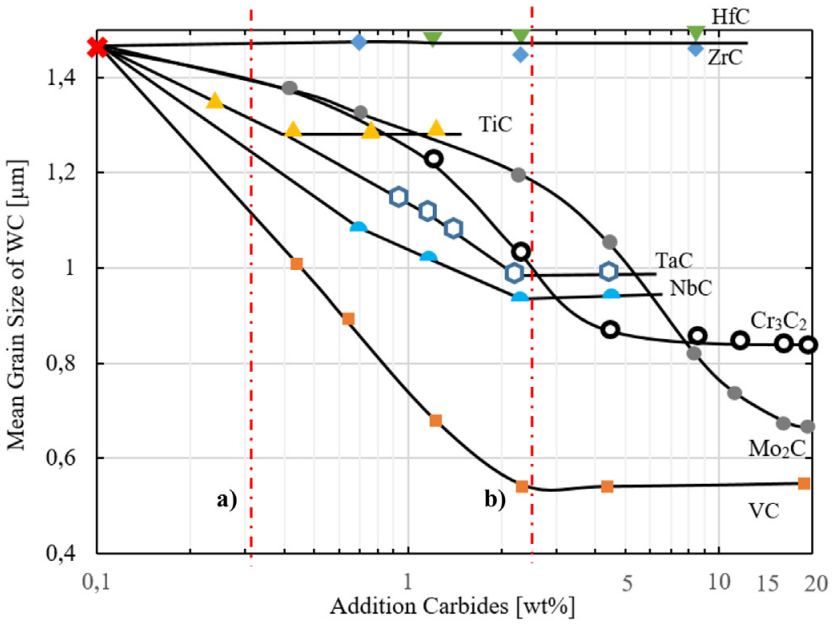

Figure 6.4: Mean WC grain size for for WC–Co materials with 20 wt% Co and varying amounts of added carbides, redrawn from Ref. 113 (data originally from Ref. 114). Here, the red dashed lines at a) and b) corresponds to low and high doping content, respectively.

6.6 Thin cubic films

6.6.1 Experimental observations

Thin cubic VC films have been observed when doping the WC–Co system with the cubic carbide VC [122, 123, 124, 116, 125, 126, 127, 128, 129, 118, 130]. These films are usually observed to be about 1 to 2 VC layers thick, but sometimes thicker films are formed. An HRTEM image of a typical VC film from is shown in Fig. 6.5.

Films have also been observed when doping with the cubic carbide TiC [121, 119, 132, 118, 130], an example of which is shown in Fig. 6.6. This Ti-rich film from the recent study, Ref. 132, shows an interesting behavior where the Ti atoms are located not in the first cubic metal layer (counted from Co) but the second. This ordering behavior was also observed in a more recent study [130]. In our atomic-scale modeling of Ti-rich films in Paper VII, we also find this ordering in our simulations. Additionally, thin TiC films have been observed inside WC grains [133].

Even in the undoped WC–Co systems cubic films have been observed [134, 108, 118], as illustrated by the HRTEM image shown in Fig. 6.7. These films are about 2 to 4

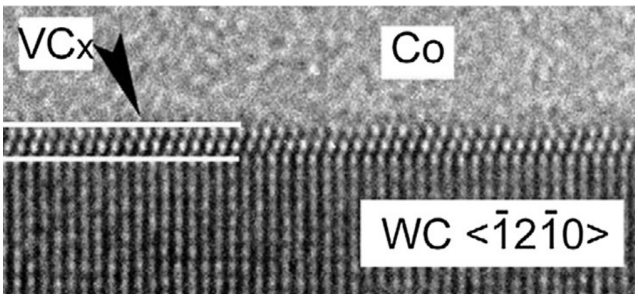

Figure 6.5: High resolution transmission electron microscopy image of a thin cubic VC film, from Ref. 131.

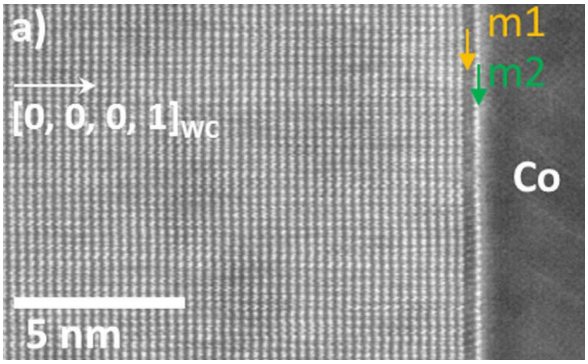

Figure 6.6: Scanning transmission electron microscopy image of a cubic TiC film, from Ref. 132.

WC layers thick and mainly observed on the WC basal plane, although Liu et al. also observed them on prismatic planes [118]. Bounhoure et al. state that cubic films in undoped WC–Co are seldom found in C-rich material, but very frequently observed in W-rich material [134]. This can be understood from the fact that the WC cubic phase contains a high concentration of carbon vacancies whereas the hexagonal WC phase is stoichiometric. In W-rich materials the carbon chemical potential is lower compared to C-rich materials, meaning that the cubic WC films (containing carbon vacancies) are more favorable in W-rich than in C-rich materials..

It is probable that the cubic films present at the WC/Co phase boundaries are related to the grain growth inhibition effect [123, 116, 117, 113, 118, 135]. Therefore, it is important to understand under which conditions these cubic films can form, e.g., in order to be able to tailor the sintering conditions to achieve a desired microstructure. It is also possible that, rather than forming complete films, individual dopant atoms segregate to WC grains and thus partially inhibit growth as discussed in Ref. 136.

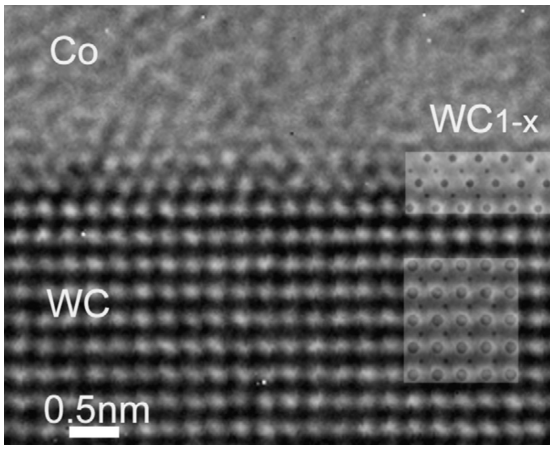

Figure 6.7: High resolution transmission electron microscopy image of a two layer thick cubic film at the phase boundary between the basal WC plane and Co from Ref. 134.

6.6.2 Simplified modeling of thin cubic films

The interface energy of thin cubic films in WC–Co can to a large extent be understood from a simplified model as demonstrated in Ref. 137 using DFT calculations. The formation of a film can be thought of inserting a thin region of stoichiometric cubic MC phase at the phase boundary between WC and Co, as illustrated in Fig. 6.8. The system

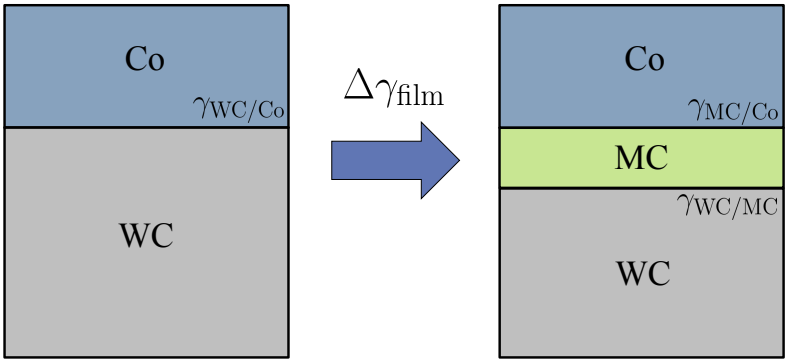

Figure 6.8: Schematic representation of the creation of a thin film. Here, MC represents a cubic carbide film with, for example, M=(W, Ti, V).

goes from having one interface WC/Co to having two, WC/MC and MC/Co. In order for the film to be stable it is necessary that the sum of two latter interface energies is

lower than the starting interface energy, i.e.

$$\gamma_{\mathrm{WC/MC}} + \gamma_{\mathrm{MC/Co}} < \gamma_{\mathrm{WC/Co}}, \tag{6.1}$$

where $\gamma_{\mathrm{X/Y}}$ denotes the interface energy between two phases X and Y. For convenience $\Gamma = \gamma_{\mathrm{WC/MC}} + \gamma_{\mathrm{MC/Co}} - \gamma_{\mathrm{WC/Co}}$ is introduced, which corresponds to the change in interface energies when inserting a film. Even if $\Gamma < 0$, creating the film also comes with an associated cost of creating the MC phase of $\Delta g_{\mathrm{MC}} + e_{\mathrm{MC}}$ per MC-layer. Here, Δg_{MC} denotes the cost of creating the cubic MC phase compared to the equilibrium phases and e_{MC} denotes the strain energy associated with the misfit between the hexagonal WC phase and the film. In total, a film of N MC-layers is stable if the formation energy of the film, $\Delta\gamma_{\mathrm{film}}$, defined as

$$\begin{aligned} \Delta\gamma_{\mathrm{film}}(N) &= \gamma_{\mathrm{WC/MC}} + \gamma_{\mathrm{MC/Co}} + N(\Delta g_{\mathrm{MC}} + e_{\mathrm{MC}}) - \gamma_{\mathrm{WC/Co}} && (6.2)\\ &= \Gamma + N(\Delta g_{\mathrm{MC}} + e_{\mathrm{MC}}) && (6.3) \end{aligned}$$

is negative. This estimate of the formation energy of the film becomes less reliable when N is small.

Relevant energies in the simplified model are shown in Table 6.2 for V and Ti doped [138] as well as undoped films. Here, we assume equilibrium with graphite, hexagonal WC and stoichiometric cubic carbide MC. The film is placed on the basal plane with the orientation

$$\delta\text{-WC}(0001) \parallel \gamma\text{-WC}(111) \parallel \mathrm{Co}(111), \tag{6.4}$$

where δ-WC and γ-WC corresponds to the hexagonal and cubic phases, respectively. It is clear from Table 6.2 that all three films fulfill Eq. (6.1), i.e. $\Gamma < 0$. For V and Ti we assume equilibrium with the stoichiometric cubic carbide MC, and hence $\Delta g = 0$. For the V films, $\Delta\gamma_{\mathrm{film}}$ (assuming two MC layers) is negative, meaning VC films are predicted to be stable. In the case of Ti, a small but positive value is obtained, indicating the possibility of TiC film formation.

The simplified models for these three cases (W, Ti, V) are shown together with explicit calculations of film energies with varying thickness in Fig. 6.9. Here, explicit calculations refer to DFT calculations carried out for atomistic WC/Co systems with a stoichiometric MC film. It is apparent that the simplified model works quite well compared to the explicit calculations and gives a good qualitative, possibly even semi-quantitative, description of film formations energies. For very thin films ($N < 2$), the separation into two distinct interfaces and a bulk region becomes questionable and one can expect the simplified model to be less accurate and reliable. This can be seen in Fig. 6.9 for $N = 1$ in the case of V.

So far, we have treated the thin cubic films with the simplified model at 0 K, neglecting any temperature effects. From the W–C phase diagram [92] and analysis done in

Paper V, it is clear γ-WC has a strong vibrational contribution to the free energy, making it thermodynamically stable at about 3000 K. Additionally, for most cubic carbides the ground-state structure will be a mixed phase, e.g., (W, Ti)C_x, when in equilibrium with δ-WC, rather than a stoichiometric MC phase. In order to understand the interface properties of a mixed (W, Ti)C_x film at finite temperatures one must turn to more extensive atomic-scale modeling.

M	$\gamma_{\mathrm{WC/Co}}$	$\gamma_{\mathrm{WC/MC}}$	$\gamma_{\mathrm{MC/Co}}$	Γ	e_{MC}	Δg_{MC}	$\Delta\gamma_{\mathrm{film}}(N=2)$
V	1.13	0.03	−0.01	−1.11	0.01	0.00	−1.09
Ti	1.13	−0.34	0.86	−0.61	0.40	0.00	0.19
W	1.13	0.45	−1.3	−1.98	0.44	2.0	2.9

Table 6.2: Relevant interface energies and associated cost for creating the cubic phase for V, Ti, and W. Here, WC refers to the hexagonal WC phase (δ-WC) and MC to the cubic carbide phase. All interfaces are metal terminated. All values are given in J/m^2.

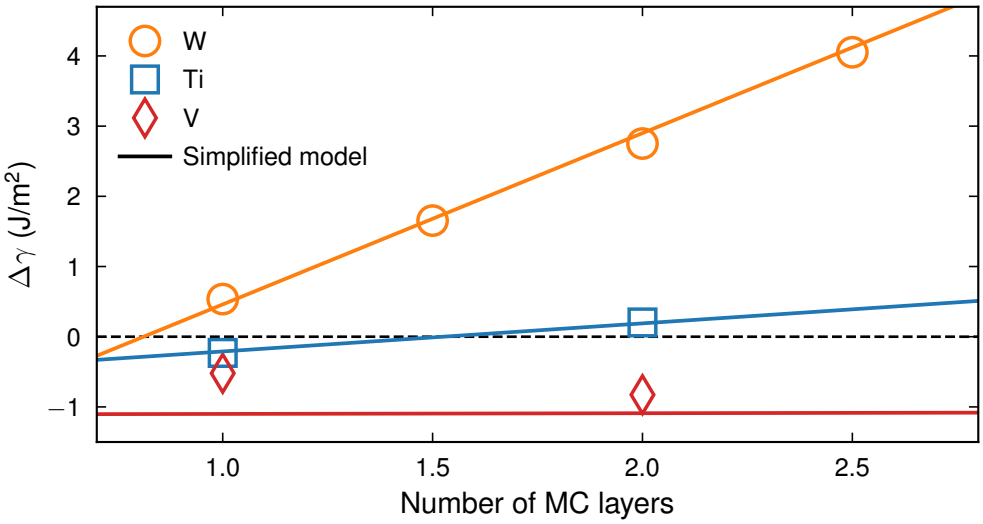

Figure 6.9: Simplified model for the formation energies of thin cubic films for M=W, Ti, V. Explicit calculations of thin film energies are marked by symbols.

6.6.3 Extensive modeling

For the undoped cubic films, the formation energy for $N = 2$ is very large, 2.9 J/m^2, yet these films are frequently observed in experimental studies [134, 118]. In order

to understand this apparent contradiction, we employ CEs to model the configurational DOFs associated with the presence of C vacancies and harmonic force constants to model the vibrational DOFs in Paper VI. Our work builds upon the work done by Johansson et al. Ref. 43, which used CEs to study cubic (W,V)C films. We find that undoped cubic films are indeed thermodynamically stable, but only at high temperatures and low carbon chemical potentials. In Paper VII, a similar methodology is employed, also including W→Ti substitution in order to model a (W,Ti)C_x film. We construct the phase diagram for Ti-rich thin cubic films and predict the same ordering in the films as experimentally observed (shown in Fig. 6.6).

7

Summary of papers

Paper I and II

In Paper I, the HIPHIVE package is presented. The formalism for how force constants can be parameterized using label symmetries, crystal symmetries, and different sum rules is introduced. The workflow of and core objects in HIPHIVE are explained and the usage of HIPHIVE is demonstrated through three examples. In the first example second and third-order force constants are extracted for a monolayer of MoS_2. The force constant extraction is shown to converge very quickly with the number of training structures; accurate thermal conductivity, for example, can be obtained using only a few tens of structures whereas using the direct approach requires several hundred. The regression approach also works very efficiently for extracting second-order force constants for system with large unit cells and low symmetry as demonstrated in the second example, which considers the vibrational spectrum of a S vacancy in a monolayer of MoS_2. In the third example we show how a fourth-order model can be used in MD simulations to account for anharmonic effects in dynamical properties such as the mean squared displacements.

In Paper II, we focus on getting a better understanding of the best practices for force constant extraction using regression techniques. We analyze how sensitive thermodynamic and transport properties are with respect to the accuracy of the force constants and demonstrate how fourth-order models can be used to account for strong anharmonicity and sampled with MD simulations.

Paper III

In Paper III, the ICET package is introduced. The general formalism of alloy CE is explained, and the workflow and features of ICET are presented. The construction of CE models is discussed in detail with respect to different regression methods. Finally, two examples are show in order to demonstrate the usage of ICET. The first one addresses the construction of the phase diagram of the binary Ag–Pd face-centered cubic (FCC) system via free energy sampling using MC simulations. In the second example the chemical ordering of the inorganic clathrate $Ba_8Al_xSi_{46-x}$ is studied as a function of temperature.

Paper IV

The interface energies of WC–Co cemented carbides are important for understanding and predicting the microstructure of the material, which is strongly related to the mechanical properties of the material. Interfaces in WC–Co have been extensively studied with DFT calculations and the ground-state 0 K interface energies have been computed. When sintering WC–Co one often reaches temperature above 1500 K for which the Co phase melts and thus the interface energies can change substantially.

In Paper IV, the temperature dependency of interface free energies is studied for various different interfaces in the WC–Co system using an ABOP. This is done as a function of temperature up to and beyond the melting point of Co. We use a few different free energy calculation methods. The calculations for the solid-liquid WC–Co interfaces prove rather challenging. To this end, we employ simulations where the two phase (WC and Co) are initially separated and then slowly brought into contact with each other. We find that most of the interface free energies studied decrease by about 10-20% at 2000 K compared to 0 K. This provide a good complement to previous DFT calculations of interface energies.

Paper V

In Paper V, we investigate the thermodynamic properties and free energies of the cubic (γ-WC) and hexagonal (δ-WC) bulk WC phases as function of both composition and temperature. In order to study these phases we include configurational, vibrational, and electronic DOFs with the help of ICET and HIPHIVE.

The hexagonal phase contains less than 1% C vacancies at 3000 K, and thus the configurational DOFs can be modelled in the dilute limit. From experimental studies it is known that the cubic phase may, however, contain up to 50% C vacancies and is only thermodynamically stable at temperatures close to melting. We employ CEs for the carbon-vacancy sub-lattice of the cubic phase. The CE is used for sampling the config-

urational free energy in the semi-grand canonical (SGC) ensemble as well as to generate both ground-state structures and representative structures at high temperatures.

The cubic phase is revealed to be dynamically unstable in the harmonic approximation at stoichiometric composition, but stable when introducing about 25% carbon vacancies. This demonstrates the non-trivial coupling between the configurational and vibrational DOFs of the cubic phase. The cubic phase is further treated with EHMs, which are constructed from ab-initio MD simulations at various temperatures. The vibrational mixing free energy is calculated across the concentration range and is found to have a strong concentration dependency. We also find that there is a significant difference in vibrational free energy between the ground-state and the representative structures.

Finally, the W–C phase diagram, for the two WC phases studied, is constructed from the total free energies. Our calculated transition temperature between the hexagonal and cubic phase is about 5 to 10% lower than in experimental studies but the overall qualitative picture is in good agreement. While the electronic free energy is smaller compared to configurational and vibrational free energies, we demonstrate that all DOFs are important to understand the thermodynamic stability of the cubic phase. We also note that thermal expansion has a non-negligible effect on the final free energies and the phase diagram. We show that the cubic phase has many ordered low-temperature structures, e.g. W_8C_7 and W_8C_4, similar to other transition metal carbides which may be of importance when considering, e.g., cubic interfacial structures or nanoparticles at lower temperatures.

Paper VI

In Paper VI, we employ computational methods in order to study the thermodynamics of thin cubic films at a WC–Co phase boundary. Many different possible stacking sequences of the cubic film with varying thickness are considered. We model carbon vacancies in the thin cubic film using CEs. The configurational free energy is sampled using MC simulations. Further, we compute the vibrational properties of the thin cubic films for the ground-state structures as a function of carbon vacancy concentration using the harmonic approximation and force constant extraction with HIPHIVE. This allows us to construct the interface free energies of the thin cubic films as function of both carbon chemical potential and temperature, which enables the interfacial phase diagram to be constructed.

We predict that thin cubic films are thermodynamically stable for high temperatures and in W-rich conditions. This is in good qualitative agreement with experimental observations from transmission electron microscopy studies. Finally, we provide a discussion of how the presence of films could effect WC grain growth. This provides a possible explanation for the experimental observation that grain growth is slower in

W-rich than in C-rich materials.

Paper VII

In Paper VII, we use the same computational method as in Paper VI but apply it to study thin cubic films in Ti doped WC–Co. The calculated interfacial free energies of Ti-rich cubic films are coupled to thermodynamic databases. This allows us to calculate the interfacial phase diagram as a function of Ti and C composition in a W–C–Ti–Co system, making it more relevant and comparable to experimental work. We find that Ti atoms only segregate to the inner metallic layer of the thin cubic film, leaving an almost pure W layer at the Co interface, an ordering which has been observed in recent experimental HRTEM studies.

8

Outlook

Atomic-scale models have been used throughout this thesis, although training these models is not always a trivial task. Software packages such as ICET and HIPHIVE help with making model construction easier, but still require some effort from the user. In the future, automated protocols, partly based on insight gained in this work, can hopefully be developed in order to simplify this process and accessible even for non-experts.

Modeling both configurational and vibrational DOFs and the coupling between them with CEs and force constants is computationally expensive. Here, one could consider exploring how to more effectively obtain the force constants for each configuration. When there the coupling between configurational and vibrational DOFs is strong, it could, however, be more efficient to train a general interatomic potential.

In regards to force constants potentials, there is an open question about how to make the potential stable such that long (ns time scale) MD simulations can be performed close to the melting temperature. If there was a general solution to this problem, higher-order models could become more widely used for efficient sampling of thermodynamic properties of materials.

The atomistic mechanism behind the gradual grain growth inhibition with increasing dopant concentrations (V, Ti, Cr, ...) in cemented carbide is still an open question. While thin cubic films at WC–Co phase boundaries appear to slow down grain growth, this is likely not the full picture. Another possible explanation that would be worth further exploration is the partial segregation of dopants to phase boundaries. Further, it is possible that segregation energies to steps is favorable and could slow down grain growth even even in the absence of films. These are ideas that could be explored with atomic-scale simulations.

Additionally, atomic-scale simulations could be used to try to estimate free energy barriers for grain growth processes such as nucleation and lateral growth. These types of calculations could lead to an estimate of the change of rates with respect to param-

eters such as carbon content, temperature, presence of a film, and partial segregation. This would help connect simulations even more directly to the grain growth rate observed in real materials.

Acknowledgments

Firstly I would I like to thank my main supervisor Göran Wahnström for his support and guidance. Also thank you for pushing me to get this thesis written, it was definitely needed. I would also like to thank my co-supervisor Paul Erhart for all the inspiring discussions throughout the years.

Thank you to my office mate and good friend Mattias Ångqvist for always making the office hours entertaining in various ways.

Thank you to Martin Gren for introducing me to the cemented carbide projects, all long fruitful discussions and for always helping me out.

Thanks to Fredrik Eriksson for making the development of HIPHIVE very enjoyable.

Thank you to all current and former colleagues in the Condensed Matter and Materials Theory group for providing such a great and motivating work environment.

Thank you to our collaborators from the SSF sintering project at KTH, Sandvik, Seco Tools and Grenoble INP for all the interesting and inspiring discussions.

Lastly, I would like to thank my parents and sister for their support over the years, it means the world.

Bibliography

[1] A. H. Larsen, J. J. Mortensen, J. Blomqvist, I. E. Castelli, R. Christensen, M. Dułak, J. Friis, M. N. Groves, B. Hammer, C. Hargus, E. D. Hermes, P. C. Jennings, P. B. Jensen, J. Kermode, J. R. Kitchin, E. L. Kolsbjerg, J. Kubal, K. Kaasbjerg, S. Lysgaard, J. B. Maronsson, T. Maxson, T. Olsen, L. Pastewka, A. Peterson, C. Rostgaard, J. Schiøtz, O. Schütt, M. Strange, K. S. Thygesen, T. Vegge, L. Vilhelmsen, M. Walter, Z. Zeng, and K. W. Jacobsen, *The atomic simulation environment—a Python library for working with atoms*, Journal of Physics: Condensed Matter **29**, 273002 (2017).

[2] A. Stukowski, *Visualization and analysis of atomistic simulation data with OVITO–the Open Visualization Tool*, Modelling and Simulation in Materials Science and Engineering **18**, 015012 (2009).

[3] P. Hohenberg and W. Kohn, *Inhomogeneous Electron Gas*, Physical Review **136**, B864 (1964).

[4] R. M. Martin, *Electronic Structure: Basic Theory and Practical Methods* (Cambridge University Press, Cambridge, 2004).

[5] R. O. Jones, *Density functional theory: Its origins, rise to prominence, and future*, Review of Modern Physics **87**, 897 (2015).

[6] S. Curtarolo, G. L. W. Hart, M. B. Nardelli, N. Mingo, S. Sanvito, and O. Levy, *The high-throughput highway to computational materials design*, Nature Materials **12**, 191 (2013).

[7] O. A. von Lilienfeld and K. Burke, *Retrospective on a decade of machine learning for chemical discovery*, Nature Communications **11**, 4895 (2020).

[8] H. E. Exner, *Physical and Chemical Nature of Cemented Carbides*, International Materials Reviews **24**, 149 (1979).

[9] H.-O. Andrén, *Microstructures of cemented carbides*, Materials Design **22**, 491 (2001).

[10] J. García, V. C. Ciprés, A. Blomqvist, and B. Kaplan, *Cemented carbide microstructures: a review*, International Journal of Refractory Metals and Hard Materials **80**, 40 (2019).

[11] G. S. Upadhyaya, *Cemented Tungsten Carbides: Production, Properties, and Testing*, 1 ed. (Noyes Publications, Westwood, NJ, 1998).

[12] L. Prakash, *1.02 - Fundamentals and General Applications of Hardmetals*, in *Comprehensive Hard Materials*, edited by V. K. Sarin (Elsevier, Oxford, 2014).

[13] S. Lay and J.-M. Missiaen, *1.03 - Microstructure and Morphology of Hardmetals*, in *Comprehensive Hard Materials*, edited by V. K. Sarin (Elsevier, Oxford, 2014).

[14] M. Christensen, S. Dudiy, and G. Wahnström, *First-principles simulations of metal-ceramic interface adhesion: Co/WC versus Co/TiC*, Physical Review B **65**, 045408 (2002).

[15] M. Christensen and G. Wahnström, *Effects of cobalt intergranular segregation on interface energetics in WC–Co*, Acta Materialia **52**, 2199 (2004).

[16] M. Christensen, G. Wahnström, C. Allibert, and S. Lay, *Quantitative Analysis of WC Grain Shape in Sintered WC-Co Cemented Carbides*, Physical Review Letters **94**, 066105 (2005).

[17] Y. Zhong, H. Zhu, L. L. Shaw, and R. Ramprasad, *The equilibrium morphology of WC particles – A combined ab initio and experimental study*, Acta Materialia **59**, 3748 (2011).

[18] M. V. G. Petisme, S. A. E. Johansson, and G. Wahnström, *A computational study of interfaces in WC–Co cemented carbides*, Modelling and Simulation in Materials Science and Engineering **23**, 045001 (2015).

[19] M. A. Gren and G. Wahnström, *Wetting of surfaces and grain boundaries in cemented carbides and the effect from local chemistry*, Materialia **8**, 100470 (2019).

[20] M. P. Allen and D. J. Tildesley, *Computer simulation of liquids.*, *Oxford Science Publications* (Clarendon Press, Oxford, 1987).

[21] D. Frenkel and B. Smit, *Understanding Molecular Simulation: From Algorithms to Applications* (Academic Press, San Diego, 2001).

[22] M. E. Tuckerman, *Statistical mechanics : theory and molecular simulation.*, *Oxford graduate texts* (Oxford University Press, Oxford, 2010).

[23] G. Ceder, *A derivation of the Ising model for the computation of phase diagrams*, Computational Materials Science **1**, 144 (1993).

[24] A. van de Walle and G. Ceder, *The effect of lattice vibrations on substitutional alloy thermodynamics*, Review of Modern Physics **74**, 11 (2002).

[25] J. Maier, *Physical chemistry of ionic materials : ions and electrons in solids* (John Wiley, Chichester, England Hoboken, NJ, 2004).

[26] A. Sutton and R. Balluffi, *Interfaces in crystalline materials*, *Monographs on the physics and chemistry of materials* (Clarendon Press, Oxford, 1995).

[27] J. M. Sanchez, F. Ducastelle, and D. Gratias, *Generalized Cluster Description of Multicomponent Systems*, Physica A: Statistical Mechanics and its Applications **128**, 334 (1984).

[28] K. P. Murphy, *Machine learning: a probabilistic perspective* (The MIT Press, Cambridge, Mass. [u.a.], 2012).

[29] L. J. Nelson, V. Ozoliņš, C. S. Reese, F. Zhou, and G. L. W. Hart, *Cluster Expansion Made Easy with Bayesian Compressive Sensing*, Physical Review B **88**, 155105 (2013).

[30] T. Mueller and G. Ceder, *Bayesian approach to cluster expansions*, Physical Review B **80**, 024103 (2009).

[31] B. Efron, *Second Thoughts on the Bootstrap*, Statistical Science **18**, 135 (2003).

[32] D. Kleiven, J. Akola, A. A. Peterson, T. Vegge, and J. H. Chang, *Training sets based on uncertainty estimates in the cluster-expansion method*, Journal of Physics: Energy **3**, 034012 (2021).

[33] E. J. Candes and M. B. Wakin, *An Introduction To Compressive Sampling*, IEEE Signal Processing Magazine **25**, 21 (2008).

[34] L. J. Nelson, G. L. W. Hart, F. Zhou, and V. Ozoliņš, *Compressive Sensing as a Paradigm for Building Physics Models*, Physical Review B **87**, 035125 (2013).

[35] H. Akaike, *A New Look at the Statistical Model Identification*, IEEE Transactions on Automatic Control **19**, 716 (1974).

[36] G. Schwarz, *Estimating the Dimension of a Model*, The Annals of Statistics **6**, 461 (1978).

[37] K. Aho, D. Derryberry, and T. Peterson, *Model Selection for Ecologists: The Worldviews of AIC and BIC*, Ecology **95**, 631 (2014).

[38] J. Zhang, X. Liu, S. Bi, J. Yin, G. Zhang, and M. Eisenbach, *Robust Data-Driven Approach for Predicting the Configurational Energy of High Entropy Alloys*, Materials & Design **185**, 108247 (2020).

[39] J. M. Rahm, J. Löfgren, E. Fransson, and P. Erhart, *A tale of two phase diagrams: Interplay of ordering and hydrogen uptake in Pd–Au–H*, Acta Materialia **211**, 116893 (2021).

[40] P. Ekborg-Tanner and P. Erhart, *Hydrogen-driven Surface Segregation in Pd-alloys from Atomic Scale Simulations*, Journal of Physical Chemistry C **ASAP**, (2021), 10.1021/acs.jpcc.1c00575.

[41] https://gitlab.com/erikfransson/fitting-examples/, Accessed: 2021-06-31.

[42] K. Frisk, *A Revised Thermodynamic Description of the Ti–C System*, Calphad **27**, 367 (2003).

[43] S. A. E. Johansson and G. Wahnström, *First-Principles Study of an Interfacial Phase Diagram in the V-Doped WC-Co System*, Physical Review B **86**, 035403 (2012).

[44] K. Parlinski, Z. Q. Li, and Y. Kawazoe, *First-Principles Determination of the Soft Mode in Cubic ZrO_2*, Physical Review Letters **78**, 4063 (1997).

[45] A. Togo and I. Tanaka, *First Principles Phonon Calculations in Materials Science*, Scripta Materialia **108**, 1 (2015).

[46] A. Togo, L. Chaput, and I. Tanaka, *Distributions of Phonon Lifetimes in Brillouin Zones*, Physical Review B **91**, 094306 (2015).

[47] W. Li, J. Carrete, N. A. Katcho, and N. Mingo, *ShengBTE: A Solver of the Boltzmann Transport Equation for Phonons*, Computer Physics Communications **185**, 1747 (2014).

[48] T. Tadano, Y. Gohda, and S. Tsuneyuki, *Anharmonic force constants extracted from first-principles molecular dynamics: applications to heat transfer simulations*, Journal of Physics: Condensed Matter **26**, 225402 (2014).

[49] J. Carrete, B. Vermeersch, A. Katre, A. van Roekeghem, T. Wang, G. K. H. Madsen, and N. Mingo, *almaBTE : A Solver of the Space–Time Dependent Boltzmann Transport Equation for Phonons in Structured Materials*, Computer Physics Communications **220**, 351 (2017).

[50] J. J. Plata, P. Nath, D. Usanmaz, J. Carrete, C. Toher, M. de Jong, M. Asta, M. Fornari, M. B. Nardelli, and S. Curtarolo, *An Efficient and Accurate Framework for Calculating Lattice Thermal Conductivity of Solids: AFLOW—AAPL Automatic Anharmonic Phonon Library*, npj Computational Materials **3**, 45 (2017).

[51] K. Esfarjani and H. T. Stokes, *Method to Extract Anharmonic Force Constants from First Principles Calculations*, Physical Review B **77**, 144112 (2008).

[52] K. Esfarjani, G. Chen, and H. T. Stokes, *Heat Transport in Silicon from First-Principles Calculations*, Physical Review B **84**, 085204 (2011).

[53] O. Hellman, P. Steneteg, I. A. Abrikosov, and S. I. Simak, *Temperature Dependent Effective Potential Method for Accurate Free Energy Calculations of Solids*, Physical Review B **87**, 104111 (2013).

[54] F. Zhou, W. Nielson, Y. Xia, and V. Ozoliņš, *Lattice Anharmonicity and Thermal Conductivity from Compressive Sensing of First-Principles Calculations*, Physical Review Letters **113**, 185501 (2014).

[55] F. Zhou, W. Nielson, Y. Xia, and V. Ozoliņš, *Compressive sensing lattice dynamics. I. General formalism*, Physical Review B **100**, 184308 (2019).

[56] F. Zhou, B. Sadigh, D. Åberg, Y. Xia, and V. Ozoliņš, *Compressive sensing lattice dynamics. II. Efficient phonon calculations and long-range interactions*, Physical Review B **100**, 184309 (2019).

[57] T. Tadano and S. Tsuneyuki, *Quartic Anharmonicity of Rattlers and Its Effect on Lattice Thermal Conductivity of Clathrates from First Principles*, Physical Review Letters **120**, 105901 (2018).

[58] T. Tadano and S. Tsuneyuki, *First-Principles Lattice Dynamics Method for Strongly Anharmonic Crystals*, Journal of the Physical Society of Japan **87**, 041015 (2018).

[59] D. C. Wallace, *Thermodynamics of Crystals* (Dover, Mineola, New York, 1998).

[60] B. Fultz, *Vibrational thermodynamics of materials*, Progress in Materials Science **55**, 247 (2010).

[61] M. V. G. Petisme, S. A. E. Johansson, and G. Wahnström, *A Computational Study of Interfaces in WC–Co Cemented Carbides*, Modelling and Simulation in Materials Science and Engineering **23**, 045001 (2015).

[62] O. Hellman, I. A. Abrikosov, and S. I. Simak, *Lattice dynamics of anharmonic solids from first principles*, Physical Review B **84**, 180301 (2011).

[63] L. T. Kong, *Phonon Dispersion Measured Directly from Molecular Dynamics Simulations*, Computer Physics Communications **182**, 2201 (2011).

[64] P. Souvatzis, O. Eriksson, M. I. Katsnelson, and S. P. Rudin, *Entropy Driven Stabilization of Energetically Unstable Crystal Structures Explained from First Principles Theory*, Physical Review Letters **100**, 095901 (2008).

[65] I. Errea, M. Calandra, and F. Mauri, *Anharmonic free energies and phonon dispersions from the stochastic self-consistent harmonic approximation: Application to platinum and palladium hydrides*, Physical Review B **89**, 064302 (2014).

[66] T. Tadano and S. Tsuneyuki, *Self-Consistent Phonon Calculations of Lattice Dynamical Properties in Cubic* $SrTiO_3$ *with First-Principles Anharmonic Force Constants*, Physical Review B **92**, 054301 (2015).

[67] K. Esfarjani and Y. Liang, *Nanoscale Energy Transport*, *2053-2563* (IOP Publishing, Bristol England, 2020), pp. 7–1 to 7–35.

[68] P. Korotaev, M. Belov, and A. Yanilkin, *Reproducibility of vibrational free energy by different methods*, Computational Materials Science **150**, 47 (2018).

[69] E. Metsanurk and M. Klintenberg, *Sampling-dependent systematic errors in effective harmonic models*, Physical Review B **99**, 184304 (2019).

[70] R. W. Zwanzig, *High-Temperature Equation of State by a Perturbation Method. I. Nonpolar Gases*, The Journal of Chemical Physics **22**, 1420 (1954).

[71] T. Andersson, Master's thesis, Chalmers University of Technology, Gothenburg, Sweden, 2012, *One-shot free energy calculations for crystalline materials*.

[72] Jones J. E. and Chapman Sydney, *On the Determination of Molecular Fields. —II. From the Equation of State of a Gas*, Proceedings of the Royal Society of London. Series A, Containing Papers of a Mathematical and Physical Character **106**, 463 (1924).

[73] M. S. Daw and M. I. Baskes, *Embedded-Atom Method: Derivation and Application to Impurities, Surfaces, and Other Defects in Metals*, Physical Review B **29**, 6443 (1984).

[74] J. K. Nørskov, *Covalent Effects in the Effective-Medium Theory of Chemical Binding: Hydrogen Heats of Solution in the* 3*d Metals*, Physical Review B **26**, 2875 (1982).

[75] M. W. Finnis and J. E. Sinclair, *A Simple Empirical N-Body Potential for Transition Metals*, Philosophical Magazine A **50**, 45 (1984).

[76] G. C. Abell, *Empirical Chemical Pseudopotential Theory of Molecular and Metallic Bonding*, Physical Review B **31**, 6184 (1985).

[77] J. Tersoff, *New Empirical Approach for the Structure and Energy of Covalent Systems*, Physical Review B **37**, 6991 (1988).

[78] D. W. Brenner, *Empirical Potential for Hydrocarbons for Use in Simulating the Chemical Vapor Deposition of Diamond Films*, Physical Review B **42**, 9458 (1990).

[79] N. Juslin, P. Erhart, P. Träskelin, J. Nord, K. O. E. Henriksson, K. Nordlund, E. Salonen, and K. Albe, *Analytical Interatomic Potential for Modeling Nonequilibrium Processes in the W–C–H System*, Journal of Applied Physics **98**, 123520 (2005).

[80] M. Petisme, M. Gren, and G. Wahnström, *Molecular dynamics simulation of WC/WC grain boundary sliding resistance in WC-Co cemented carbides at high temperature*, International Journal of Refractory Metals and Hard Materials **49**, 75 (2015).

[81] L. Verlet, *Computer "Experiments" on Classical Fluids. I. Thermodynamical Properties of Lennard-Jones Molecules*, Physical Review **159**, 98 (1967).

[82] J. G. Kirkwood, *Statistical Mechanics of Fluid Mixtures*, The Journal of Chemical Physics **3**, 300 (1935).

[83] D. Frenkel and A. J. C. Ladd, *New Monte Carlo Method to Compute the Free Energy of Arbitrary Solids. Application to the Fcc and Hcp Phases of Hard Spheres*, The Journal of Chemical Physics **81**, 3188 (1984).

[84] R. Freitas, M. Asta, and M. de Koning, *Nonequilibrium Free-Energy Calculation of Solids Using LAMMPS*, Computational Materials Science **112**, 333 (2016).

[85] M. S. Sellers, M. Lísal, and J. K. Brennan, *Free-energy calculations using classical molecular simulation: application to the determination of the melting point and chemical potential of a flexible RDX model*, Physical Chemistry Chemical Physics **18**, 7841 (2016).

[86] R. Ravelo, T. C. Germann, O. Guerrero, Q. An, and B. L. Holian, *Shock-Induced Plasticity in Tantalum Single Crystals: Interatomic Potentials and Large-Scale Molecular-Dynamics Simulations*, Physical Review B **88**, 134101 (2013).

[87] M. I. Mendelev and Y. Mishin, *Molecular dynamics study of self-diffusion in bcc Fe*, Physical Review B **80**, 144111 (2009).

[88] D. Smirnova, S. Starikov, G. D. Leines, Y. Liang, N. Wang, M. N. Popov, I. A. Abrikosov, D. G. Sangiovanni, R. Drautz, and M. Mrovec, *Atomistic description of self-diffusion in molybdenum: A comparative theoretical study of non-Arrhenius behavior*, Physical Review Materials **4**, 013605 (2020).

[89] S. Norgren, J. García, A. Blomqvist, and L. Yin, *Trends in the P/M Hard Metal Industry*, International Journal of Refractory Metals and Hard Materials **48**, 31 (2015).

[90] Z. Zak Fang and M. C. Koopman, *1.04 - Cemented Tungsten Carbide Hardmetal - An Introduction*, in *Comprehensive Hard Materials*, edited by V. K. Sarin (Elsevier, Oxford, 2014).

[91] A. F. Guillermet, *Thermodynamic Properties of the Co-W-C System*, Metallurgical Transactions A **20**, 935 (1989).

[92] A. S. Kurlov and A. I. Gusev, *Tungsten Carbides and W-C Phase Diagram*, Inorganic Materials **42**, 121 (2006).

[93] J. Hu, C. Li, F. Wang, and W. Zhang, *Thermodynamic Re-Assessment of the V–C System*, Journal of Alloys and Compounds **421**, 120 (2006).

[94] M. Christensen, G. Wahnström, C. Allibert, and S. Lay, *Quantitative Analysis of WC Grain Shape in Sintered WC-Co Cemented Carbides*, Physical Review Letters **94**, 066105 (2005).

[95] Z. Z. Fang, X. Wang, T. Ryu, K. S. Hwang, and H. Y. Sohn, *Synthesis, Sintering, and Mechanical Properties of Nanocrystalline Cemented Tungsten Carbide – A Review*, International Journal of Refractory Metals and Hard Materials **27**, 288 (2009).

[96] M. Kahlweit, *Ostwald Ripening of Precipitates*, Advances in Colloid and Interface Science **5**, 1 (1975).

[97] C. Allibert, *Sintering features of cemented carbides WC–Co processed from fine powders*, International Journal of Refractory Metals and Hard Materials **19**, 53 (2001).

[98] O. Lavergne and C. H. Allibert, *Dissolution mechanism of tungsten carbide in cobalt-based liquids*, High Temperatures. High Pressures **31**, 347 (1999).

[99] C. H. Allibert, *Sintering features of cemented carbides WC-Co processed from fine powders*, International Journal of Refractory Metals and Hard Materials **19**, 53 (2001).

[100] K. Mannesson, J. Jeppsson, A. Borgenstam, and J. Ågren, *Carbide grain growth in cemented carbides.*, Acta Materialia **59**, 1912 (2011).

[101] Z. Roulon, J. Missiaen, and S. Lay, *Carbide grain growth in cemented carbides sintered with alternative binders*, International Journal of Refractory Metals and Hard Materials **86**, 105088 (2020).

[102] Y. Park, N. Hwang, and D. Yoon, *Abnormal growth of faceted (WC) grains in a (Co) liquid matrix*, Metallurgical and Materials Transactions A **27**, 2809 (1996).

[103] G. S. Rohrer, C. L. Rohrer, and W. W. Mullins, *Coarsening of Faceted Crystals*, Journal of the American Ceramic Society **85**, 675 (2002).

[104] Y. Zhong and L. L. Shaw, *Growth mechanisms of WC in WC–5.75wt% Co*, Ceramics International **37**, 3591 (2011).

[105] M. Bonvalet, J. Odqvist, J. Ågren, and A. Borgenstam, *Modelling of Prismatic Grain Growth in Cemented Carbides*, International Journal of Refractory Metals and Hard Materials **78**, 310 (2019).

[106] H. Suzuki, M. Sugiyama, and T. Umeda, *Effect of the carbon content on properties of WC-10%Co alloy*, Journal of the Japan Institute of Metals and Materials **28**, 55 (1964).

[107] G. J. Rees and B. Young, *A study of the factors controlling grain size in sintered hard-metal*, Powder Metallurgy **14**, 185 (1971).

[108] S. Lay, C. H. Allibert, M. Christensen, and G. Wahnström, *Morphology of WC Grains in WC–Co Alloys*, Materials Science and Engineering: A **486**, 253 (2008).

[109] A. Delanoë and S. Lay, *Evolution of the WC grain shape in WC–Co alloys during sintering: Effect of C content*, International Journal of Refractory Metals and Hard Materials **27**, 140 (2009).

[110] I. Borgh, P. Hedström, T. Persson, S. Norgren, A. Borgenstam, J. Ågren, and J. Odqvist, *Microstructure, grain size distribution and grain shape in WC–Co alloys sintered at different carbon activities*, International Journal of Refractory Metals and Hard Materials **43**, 205 (2014).

[111] S. Kim, S.-H. Han, J.-K. Park, and H.-E. Kim, *Variation of WC grain shape with carbon content in the WC–Co alloys during liquid-phase sintering*, Scripta Materialia **48**, 635 (2003).

[112] Y. Wang, M. Heusch, S. Lay, and C. Allibert, *Microstructure Evolution in the Cemented Carbides WC–Co I. Effect of the C/W Ratio on the Morphology and Defects of the WC Grains*, Physica Status Solidi A **193**, 271 (2002).

[113] S. Farag, I. Konyashin, and B. Ries, *The influence of grain growth inhibitors on the microstructure and properties of submicron, ultrafine and nano-structured hardmetals – A review*, International Journal of Refractory Metals and Hard Materials **77**, 12 (2018).

[114] K. Hayashi, Y. Fuke, and H. Suzuki, *Effects of Addition Carbides on the Grain Size of WC-Co Alloy*, Journal of the Japan Society of Powder and Powder Metallurgy **19**, 67 (1972).

[115] W. D. Schubert, A. Bock, and B. Lux, *General Aspects and Limits of Conventional Ultrafine WC Powder Manufacture and Hard Metal Production*, International Journal of Refractory Metals and Hard Materials **13**, 281 (1995).

[116] S. Lay, J. Thibault, and S. Hamar-Thibault, *Structure and Role of the Interfacial Layers in VC-Rich WC-Co Cermets*, Philosophical Magazine **83**, 1175 (2003).

[117] M. Kawakami and K. Kitamura, *Segregation of Dopants at WC/Co and WC/WC Interfaces in Solid-State-Sintered WC-VC-Cr_3C_2-Co Cemented Carbides*, Materials Transactions **56**, 1880 (2015).

[118] X. Liu, X. Song, H. Wang, X. Liu, F. Tang, and H. Lu, *Complexions in WC-Co Cemented Carbides*, Acta Materialia **149**, 164 (2018).

[119] J. Weidow and H.-O. Andrén, *Grain and Phase Boundary Segregation in WC–Co with TiC, ZrC, NbC or TaC Additions*, International Journal of Refractory Metals and Hard Materials **29**, 38 (2011).

[120] P. R. Cantwell, M. Tang, S. J. Dillon, J. Luo, G. S. Rohrer, and M. P. Harmer, *Grain Boundary Complexions*, Acta Materialia **62**, 1 (2014).

[121] M. Kawakami, O. Terada, and K. Hayashi, *HRTEM Microstructure and Segregation Amount of Dopants at WC/Co Interfaces in TiC and TaC Mono-Doped WC-Co Submicro-Grained Hardmetals*, Journal of the Japan Society of Powder and Powder Metallurgy **53**, 166 (2006).

[122] A. Jaroenworaluck, T. Yamamoto, Y. Ikuhara, T. Sakuma, T. Taniuchi, K. Okada, and T. Tanase, *Segregation of Vanadium at the WC/Co Interface in VC-doped WC-Co*, Journal of Materials Research **13**, 2450 (1998).

[123] T. Yamamoto, Y. Ikuhara, and T. Sakuma, *High Resolution Transmission Electron Microscopy Study in VC-Doped WC–Co Compound*, Science and Technology of Advanced Materials **1**, 97 (2000).

[124] S. Lay, S. Hamar-Thibault, and A. Lackner, *Location of VC in VC, Cr_3C_2 codoped WC–Co cermets by HREM and EELS*, International Journal of Refractory Metals and Hard Materials **20**, 61 (2002).

[125] S. Lay, M. Loubradou, and P. Donnadieu, *Ultra Fine Microstructure in WC-Co Cermet*, Advanced Engineering Materials **6**, 811 (2004).

[126] S. Lay, S. Hamar-Thibault, and M. Loubradou, *Accommodation of the Lattice Mismatch at the VCx-WC Interface*, Interface Science **12**, 187 (2004).

[127] I. Sugiyama, Y. Mizumukai, T. Taniuchi, K. Okada, F. Shirase, T. Tanase, Y. Ikuhara, and T. Yamamoto, *Formation of (W,V)Cx Layers at the WC/Co Interfaces in the VC-Doped WC–Co Cemented Carbide*, International Journal of Refractory Metals and Hard Materials **30**, 185 (2012).

[128] I. Sugiyama, Y. Mizumukai, T. Taniuchi, K. Okada, F. Shirase, T. Tanase, Y. Ikuhara, and T. Yamamoto, *Three-dimensional morphology of (W, V)C_x in VC-doped WC–Co hard metals*, Scripta Materialia **69**, 473 (2013).

[129] I. Sugiyama, Y. Mizumukai, T. Taniuchi, K. Okada, F. Shirase, T. Tanase, Y. Ikuhara, and T. Yamamoto, *Carbon content dependence of grain growth mode in VC-doped WC–Co hardmetals*, International Journal of Refractory Metals and Hard Materials **52**, 245 (2015).

[130] C. Yang, C. Hu, C. Xiang, H. Nie, X. Gu, L. Xie, J. He, W. Zhang, Z. Yu, and J. Luo, *Interfacial superstructures and chemical bonding transitions at metal-ceramic interfaces*, Science Advances **7**, 11 (2021).

[131] S. Lay, S. Hamar-Thibault, and M. Loubradou, *Accommodation of the Lattice Mismatch at the VC_x-WC Interface*, Interface Science **12**, 187 (2004).

[132] A. Meingast, E. Coronel, A. Blomqvist, S. Norgren, G. Wahnström, and M. Lattemann, *High Resolution STEM Investigation of Interface Layers in Cemented Carbides*, International Journal of Refractory Metals and Hard Materials **72**, 135 (2018).

[133] S. Lay, M. Loubradou, and W.-D. Schubert, *Structural Analysis on Planar Defects Formed in WC Platelets in Ti-Doped WC–Co*, Journal of the American Ceramic Society **89**, 3229 (2006).

[134] V. Bounhoure, S. Lay, M. Loubradou, and J.-M. Missiaen, *Special WC/Co Orientation Relationships at Basal Facets of WC Grains in WC–Co Alloys*, Journal of Materials Science **43**, 892 (2008).

[135] C. Yin, Y. Peng, J. Ruan, L. Zhao, R. Zhang, and Y. Du, *Influence of Cr_3C_2 and VC Content on WC Grain Size, WC Shape and Mechanical Properties of WC–6.0 wt. % Co Cemented Carbides*, Materials **14**, 1551 (2021).

[136] A. B. Yildiz, R. P. Babu, M. Bonvalet-Rolland, S. Busch, V. Ryukhtin, J. Weidow, S. Norgren, and P. Hedström, *Quantification of nano-scale interface structures to guide mechanistic modelling of WC grain coarsening inhibition in V-doped hard metals*, Materials & Design **207**, 109825 (2021).

[137] S. A. E. Johansson and G. Wahnström, *A Computational Study of Thin Cubic Carbide Films in WC/Co Interfaces*, Acta Materialia **59**, 171 (2011).

[138] S. A. E. Johansson and G. Wahnström, *First-Principles Derived Complexion Diagrams for Phase Boundaries in Doped Cemented Carbides*, Current Opinion in Solid State and Materials Science **20**, 299 (2016).